Draft version December 22, 2023
Typeset using LaTeX **twocolumn** style in AASTeX631

JWST Mid-infrared Spectroscopy Resolves Gas, Dust, and Ice in Young Stellar Objects in the Large Magellanic Cloud

Omnarayani Nayak,[1,2] Alec S. Hirschauer,[1] Patrick J. Kavanagh,[3] Margaret Meixner,[4] Laurie Chu,[5]
Nolan Habel,[6,4] Olivia C. Jones,[7] Laura Lenkić,[6,4] Conor Nally,[8] Megan Reiter,[9] Massimo Robberto,[1,10] and
B. A. Sargent[1,10]

[1] *Space Telescope Science Institute, 3700 San Martin Drive, Baltimore, MD 21218, USA*
[2] *NASA Goddard Space Flight Center, 8800 Greenbelt Road, Greenbelt, MD, USA*
[3] *Department of Experimental Physics, Maynooth University, Maynooth, Co Kildare, Ireland*
[4] *Jet Propulsion Laboratory, California Institute of Technology, 4800 Oak Grove Dr., Pasadena, CA 91109, USA*
[5] *Infrared Processing and Analysis Center, California Institute of Technology, 1200 E California Blvd, Pasadena, CA 91125, USA*
[6] *Stratospheric Observatory for Infrared Astronomy, NASA Ames Research Center, Mail Stop 204-14, Moffett Field, CA 94035, USA*
[7] *UK Astronomy Technology Centre, Royal Observatory, Blackford Hill, Edinburgh, EH9 3HJ, UK*
[8] *Institute for Astronomy, University of Edinburgh, Blackford Hill, Edinburgh, EH9 3HJ, UK*
[9] *Department of Physics & Astronomy, Rice University, 6100 Main St, Houston, TX 77005, USA*
[10] *Department of Physics & Astronomy, Johns Hopkins University, 3400 N. Charles St., Baltimore, MD 21218, USA*

(Received 31 December 2021; Revised; Accepted)

ABSTRACT

In this work, we present spectra of 11 young stellar objects (YSOs) taken with the Mid-Infrared Instrument (MIRI) / Medium Resolution Spectroscopy (MRS) instrument onboard the *James Webb Space Telescope* (JWST). The YSOs are located in the N79 region of the Large Magellanic Cloud (LMC), an active star forming region with hundreds of *Spitzer*- and *Herschel*-identified YSOs and host to super star cluster (SSC) candidate H72.97-69.39. The three giant molecular clouds (GMCs) in N79 (East, West, and South) have varying star formation rates and stellar populations. MRS follow-up observations of four *Spitzer*-identified YSOs in N79 East, West, and South reveal that what seemed to be a single, massive YSO is actually a cluster of YSOs. We discuss the emission and absorption lines of six YSOs which have complete or almost-complete spectral coverage from 4.9 – 27.9 μm. YSO Y3, located in N79 East, is the youngest source in this study and likely to be less than 10,000 years old inferred from the prominent CH_4, NH_3, CH_3OH, CH_3OCHO, and CO_2 ice absorption features. The most luminous source is the central ionizing YSO of SSC H72.97-69.39, Y4, which has dozens of fine-structure and H_2 emission lines. Unlike the other YSOs in this work, Y4 has no polyaromatic hydrocarbon (PAH) emission lines due to the intense ionizing radiation destroying these large carbon-chain molecules. **The mass accretion rate based on H I (7-6) line luminosity of YSOs Y1, Y2, Y4, and Y9 range between** $1.22 \times 10^{-4} - 1.89 \times 10^{-2}$ $M_\odot$ yr^{-1}**.** For the first time in the mid-infrared, we are able to resolve individual high-mass protostars forming in small clusters in an extra-galactic environment like the LMC.

1. INTRODUCTION

The formation of massive stars plays a vital role in influencing the chemistry and structure of the interstellar medium (ISM). Star formation takes place in clusters, with massive stars dominating the luminosity (Chen et al. 2009). At early stages of their formation, the high-velocity winds from outflows and jets can heat and compress the surrounding gas (van Dishoeck & Blake 1998; Bally 2016; Pabst et al. 2019, 2020). This can subsequently trigger or quench further star formation depending on the density distribution of the compressed gas (Walch et al. 2013). At later stages, ultraviolet (UV) radiation from these massive stars ionizes the surrounding ISM, creating H II regions (Beuther et al. 2007; Lopez et al. 2014; Barnes et al. 2020).

Corresponding author: Omnarayani Nayak
omnarayani.nayak@nasa.gov

The proximity (50 kpc; Feast 1999) and face-on orientation of the **Large Magellanic Cloud** (LMC) make it an ideal laboratory to study sites of massive star formation (Meixner et al. 2006). Ochsendorf et al. (2017) surveyed **young stellar objects** (YSOs) in the LMC using *Spitzer* and *Herschel* photometry and found two main **regions of star formation**: One is 30 Doradus, host to super star cluster (SSC) R136, and the other is N79, host to SSC candidate H72.97-69.39. 30 Doradus has gone through four star formation episodes in the last 25 million years (Hunter et al. 1995; Grebel & Chu 2000; De Marchi et al. 2011; Sabbi et al. 2013), whereas N79 is ramping up its star formation activity and **may** one day rival the star formation rate (SFR) and high luminosity of 30 Doradus (Ochsendorf et al. 2017).

In this work we use James Webb Space Telescope (JWST) Medium Resolution Spectroscopy (MRS) observations of star clusters and isolated YSOs in the N79 region of the LMC to better understand the effect of high-velocity stellar winds, low-velocity shocks from outflows, ultraviolet (UV) radiation, dust reprocessed radiation, and warm ionized gas pressure on the parental giant molecular cloud (GMC).

Feedback from a single O star (i.e., outflows, UV radiation, stellar winds) can change the local thermodynamic state of the ISM (van Dishoeck & Blake 1998). ALMA observations of the South GMC **which** cover a region $60'' \times 60''$ **in size**, reveal two **parsec-long** filaments colliding, **with H72.97-69.39 located in the center of this collision (Nayak et al. 2019).** [C II] observations **made** with Stratospheric Observatory for Infrared Astronomy (SOFIA) suggest the N79 South GMC is a photon-dominated region (PDR) with possible shocks exciting the CO (16-15) and CO (11-10) emission lines (Nayak et al. 2021). **In this work**, we are able to resolve the cluster of five protostars in H72.97-69.39 **with Mid-Infrared Instrument (MIRI) / Medium Resolution Spectroscopy (MRS) observations**. Additionally, we observe two other massive clusters, one in the South GMC and another in the East GMC. The source we observe in N79 West is a single protostar. Our observations reveal how multiple massive YSOs forming within a cluster affect local gas conditions.

YSOs are enshrouded by dust and gas, which serves as a reservoir during the **main initial** accretion phase (McKee & Ostriker 2007). UV radiation from the central illuminating source **is** absorbed and then re-radiated at mid- and far-infrared (IR) wavelengths (Churchwell 2002). The observed IR spectral emission and absorption lines can reveal the age, mass, and accretion properties of the central protostar as well as the temperature and ionized conditions of the surrounding ISM (Boonman et al. 2003b; Oliveira et al. 2009; Seale et al. 2009; Rigliaco et al. 2015). Our observations **in this work** reveal that objects identified as protostars with previous *Spitzer* Infrared sSpectrometer (IRS) are actually small clusters which we can now resolve with MRS.

We observe a variety of early- and late-stage YSOs in the South, East, and West GMCs. The spectral features of the six YSOs we discuss in detail include H_2 emission, polyaromatic hydrocarbon (PAH) emission, silicate absorption, and solid- and gas-phase ice absorption. Additionally, we observe for the first time rest-frame mid-IR hydrogen recombination lines associated with extra-galactic star formation with high-resolution MRS spectra.

The mid-IR H_2 originates either from UV radiation from massive stars or collisional excitation from shocks heating the molecular gas (Tielens et al. 1993; Hollenbach 1997). The same UV photons collide with PAH molecules which in turn 1) leads to the excitation of various bending and stretching modes, and 2) breaks down large-size PAH molecules into smaller ones (Tielens et al. 1993; Peeters et al. 2017). Electrons ejected from PAH molecules can further heat up the local gas, (i.e., via the photoelectric effect). Excess H_2 emission relative to PAH emission lines has been observed in active galactic nuclei (Ogle et al. 2010) and ultraluminous galaxies Higdon et al. (2006), and thought to originate from shocks. Hydrogen recombination lines are commonly used as a proxy for accretion rates in YSOs because of the empirical relationship between H I luminosity and accretion luminosity across a variety of environments (Calvet et al. 2004; Herczeg & Hillenbrand 2008). The presence of silicate and ice absorption lines with little to no H_2 and fine-structure emission lines is indicative of the very young protostars embedded within their natal gas cloud where the UV photons from the central star have yet to ionize the surrounding gas (Oliveira et al. 2013). The various emission and absorption lines identified in a spectrum indicate the age of the central protostar as well as PAH grain size distribution and ionization, plus the origin of shocks. In this

work, we further discuss and interpret the emission and absorption lines seen in YSOs in N79.

We refer to the four *Spitzer*-identified sources as W1, E1, S1, and S2 which is based on their location in the West, East, and South GMCs, respectively. We call the individual protostars **resolved with MIRI** within the *Spitzer*-identified clusters 'YSOs' with Y1 located in W1, Y2 and Y3 located in E1, Y4 - Y8 in S1, and Y9 - Y11 in S2. In this study, we present MRS observations of 11 YSOs in the N79 region of the LMC, six of which have full or nearly-full mid-IR spectral coverage from 4.9 – 27.9 μm. **The science goal of this program is to map out the excitation and physical conditions of the gas in order to better understand YSO formation at different evolutionary stages. In order to achieve our science goal,** we extract the emission and absorption lines of the six YSOs with full or nearly-full mid-IR spectral coverage and infer the conditions of the accreting protostar and the surrounding ISM. Follow-up papers will model the emission and absorption lines in greater detail.

In §2 we describe the source selection strategy and the observation details. The data processing and resulting catalog of spectral features are discussed in §3. The *Spitzer* IRS spectra and photometry of the four MRS observations are discussed in §4, while §5 goes into the details of the YSOs resolved with the JWST MRS observations. We summarize our results in §6.

2. OBSERVATION AND SOURCE SELECTION STRATEGY

We present observations of the N79 region taken with the Mid-Infrared Instrument (MIRI; Rieke et al. 2015; Wright et al. 2023) onboard JWST as part of GTO program 1235 (PI: Meixner). The observations were taken using MRS, an integral field unit (IFU) equipped with four channels (1, 2, 3, and 4). The channels cover a wavelength range of 4.90 – 7.65 μm, 7.51 – 11.70 μm, 11.55 – 17.98 μm, and 17.70 – 27.90 μm, respectively. Channels 1 and 2 have a higher spectral resolution (R = 2700 – 3700) in comparison to Channels 3 and 4 (R = 1600 – 2800). In contrast, Channels 1 and 2 have a smaller field of view (FOV, 10 – 20 square arcseconds) in comparison to Channels 3 and 4 (32 – 51 square arcseconds; Gardner et al. 2023). Each Channel is further subdivided into three sub-bands (i.e., A, B, and C) which consist of a 'SHORT', 'MEDIUM', and 'LONG' portion of the wavelength range, respectively. As each MRS Channel possesses the same three sub-bands (i.e., 1A, 1B, 1C, 2A, 2B, 2C, etc.), a full spectrum can therefore be observed with three exposures, typically accomplished within a single observation setup.

We use the MRS instrument to take observations of SSC candidate H72.97-69.39, which is a super-luminous source with L = 2.2×10^6 $L_\odot$, and three other *Spitzer*-identified massive YSO candidates in the N79 region (Ochsendorf et al. 2017). Based on their locations within the N79 South, East, and West GMCs, we label the *Spitzer*-identified YSO candidates as S1, S2, E1, and W1. W1 was observed on November 14, 2022, and E1 was observed on November 29, 2022. Observations of H72.97-69.39 **(labeled S1)** and S2 were taken on November 30, 2022. Figure 1 shows the *Spitzer* 8μm observations of the N79 region and the location of the four MRS observations.

The SSC candidate H72.97-69.39 was observed with MRS using the FASTR1 readout mode for a standard 4-point dither pattern, and an assumption that the source is extended. We use five groups/integration and five integrations/exposure with a total exposure time for the three sub-bands SHORT, MEDIUM, and LONG of 321 seconds. The three other *Spitzer*-identified sources S2, E1, and W1 are observed with the same readout mode and dither pattern. These YSO candidates are less luminous than H72.97-69.39 and therefore we use 13 groups/integration and two integrations/exposure for a total exposure time of 299 seconds per target.

MRS observations of S1, S2, and E1 show that what was observed to be a single source with *Spitzer* is actually a cluster of **two to five** less massive YSOs. Source W1, however, is an isolated YSO. There are a total of 11 YSOs within the four MRS observations. We chose a variety of early- and late-stage YSO candidates based on their spectral features seen with *Spitzer* IRS observations.

3. DATA PROCESSING

3.1. *MIRI MRS Pipeline Processing*

The JWST MRS observations were processed using pipeline version 1.11.0 with *jwst_1094.pmap* context (Bushouse et al. 2023). This pipeline version uses time-dependent photometric corrections, has the ability to set the outlier detection kernel size and threshold, and implements residual fringe correction during the spectral extraction process. We use the standard detector corrections ***calwebb_detector1*** and ***calwebb_spec2*** during Stage 1 and Stage 2 of the data reduction process (Labiano et al. 2016), with the ***residual_fringe*** step switched on. The residual fringe correction step

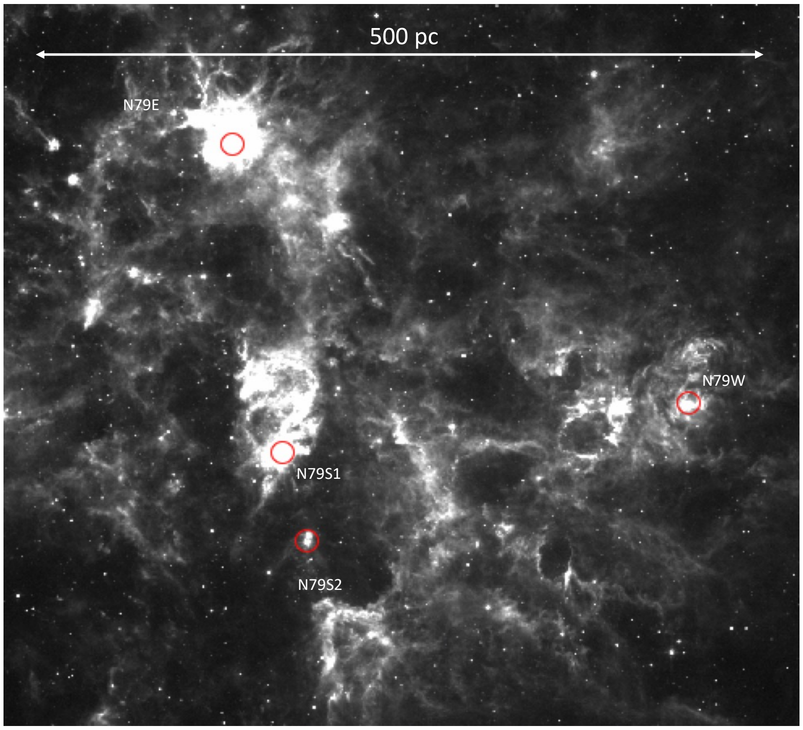

Figure 1. *Spitzer* IRAC 8.0 μm image of the N79 region. We highlight the location of the MRS footprint with the four red circles. The red circles have a diameter of $70''$, much larger than the MRS footprint. We selected these four sources because previous Spitzer IRS spectral observations indicated these are indeed YSOs, as well as SED models indicating that these YSOs are very massive (over 8 $M_\odot$).

applies additional fringe correction arising from the difference between fringe pattern on the detector from an extended source and the standard pipeline fringe flat. Stage 3 of the pipeline (***calwebb_spec3***) includes the ***outlier_detection*** and spectrum level residual fringe correction (***ifu_rfcorr***) routines. The outlier detection step compares a median taken from stacked images to the original images to determine if there are bad pixels or cosmic rays. We set the size of the kernel used to normalize the pixel difference in the outlier detection step to be 11 pixels. Even after the fringe and residual fringe corrections applied with the standard pipeline steps, there can still be fringe residuals in extracted spectra, in particular the high-frequency fringing in channels 3 and 4 thought to arise from the dichroics are often present which are difficult to remove at the detector level. We used the (***ifu_rfcorr***) step on extracted spectra to reduce the contrast of the fringes that remain.

The spectrum of each of the 11 YSOs **detected** in the four MRS pointings is extracted with an aperture defined as $1.22\lambda/D$, where λ is the wavelength of the IFU cube and D is the beam size. The background is similarly calculated by extracting a spectrum within the spectral cube, but away from the bright point sources. After background subtraction, the 12 spectral cube segments are scaled in a consecutive manner using a median flux value between two consecutive sub-bands such that channel 1B is scaled to 1A, and then channel 1C is scaled to 1B, and so forth. The resulting spectral segments are stitched together using the ***combine_1d*** step of the JWST pipeline. Figure 2 shows the MRS spectra of the 11 sources in this work as well as *Spitzer* IRS spectra of S1, S2, E1, and W1.

We fit a continuum to the spectra extracted in each sub-band using the spline function in the *astropy* package. After subtracting the continuum, the emission and absorption lines are detected with *find_lines_threshold* function from *specutils*. The lines are fit with a Gaussian profile and their parameters (measured wavelength, uncertainty in wavelength, FWHM, flux, and uncertainty in flux) are listed in Tables 1 – 6. Table 7 summarizes the emission and absorption lines seen in the spectra of Y1, Y2, Y3, Y4, Y6, and Y9. Taking into account the radial velocity of N79 (235 $\mathrm{km\,s^{-1}}$; Nayak et al. 2019), the narrow emission and absorption features are matched to the closest known H_2, HI, fine structure, or ice lines within 0.01 μm. If there are multiple matches, then the closest laboratory emission or absorption line is selected to be the observed line. The broad PAH emission line and ice absorption lines are determined by matching the observed features to the known laboratory lines with the requirement that $\lambda_{\mathrm{observed}} - \lambda_{\mathrm{laboratory}} < 0.05$. We list the emission and absorption lines we are unable to identify in Appendix Table A1, which are due to warm pixels, fringe flat correction issues, undersampling, and stitching effects in overlap channels.

3.2. *Catalog of Spectral Features*

Figures 3 – 6 show cube slices at 5.51, 6.20, 11.20, 12.81, 17.04, and 18.71 μm which trace H_2 5.51 μm, PAH features, [Ne II], H_2 17.04 μm, and [S III] emission lines, respectively. The YSOs in each region are labeled Y1 through Y11. The spectra for YSOs Y1 located in the N79 West GMC, Y2 in the East GMC, and Y4 in the South GMC observation cover the full MRS wavelength range from 4.9 – 27.9 μm. Y3 located in N79 East is very faint in Channel 1. The extracted spectrum for this source is noisy with little to no signal in wavelengths shorter than 7.5 μm. Sources Y6 in S1 and Y9 in S2 are noisy in Channel 1A and therefore the spectra shown for these two sources in Figure 2 are for 1B and longer wavelengths. YSOs Y5, Y7, and Y8 are on the edge of the MRS FOV in Channels 1 and 2 (Figure 5), therefore they do not have the full spectral coverage. Additionally, the emission lines seen in YSOs Y5, Y7, and Y8 are the same as the emission lines seen in Y6 which can be seen in Figure 2. The similarity in emission line species and line strength between the three YSOs in region S1 to Y6 implies the three protostars are not the dominating source in the MRS FOV. Y10 and Y11 are also on the edge of Channel 1 which is shown in Figure 6 and therefore do not have the full spectral coverage of MRS.

In this work we discuss sources Y1, Y2, Y3, Y4, Y6, and Y9 in further detail. Sources Y5, Y7, Y8, Y10, and Y11 are missing Channels 1 and 2 and the spectra of these sources are dominated by different nearby sources.

4. DESCRIPTION OF YSO CANDIDATES

Massive YSO candidates in the LMC have previously been identified by the *Spitzer* Surveying the Agents of Galaxy Evolution (SAGE; Meixner et al. 2006) and Herschel Inventory of the Agents of Galaxy Evolution (HERITAGE; Meixner et al. 2013) surveys. The *Spitzer* Infrared Array Camera (IRAC) and Multiband Imaging Photometer (MIPS) instruments cover a wavelength range of 3.6 – 160 μm. Galaxy-wide searches

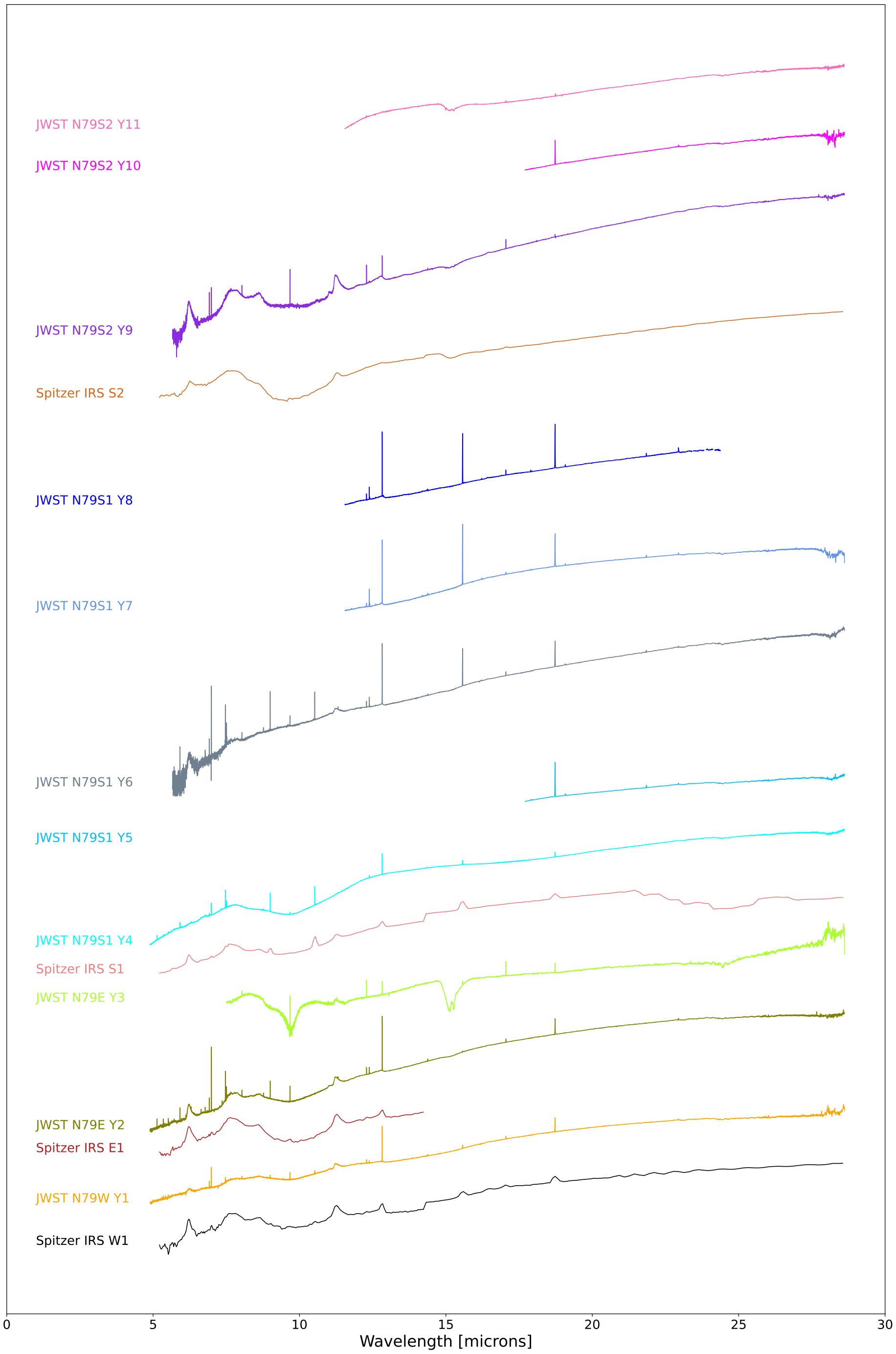

Figure 2. The *Spitzer* IRS spectra of YSOs and young massive clusters in regions **W1, E1, S1, and S2**. Spectra of MIRI/MRS sources 'Y1' through 'Y11' are also shown. The spectra are offset in an arbitrary amount such that they do not overlap with each other. Each of the *Spitzer* IRS spectrum of **W1, E1, S1, and S2** lies below the corresponding MRS spectra.

for YSO candidates, using *Spitzer* photometry implemented color-color and color-magnitude cuts, have led to the identification of approximately 1800 YSO candidates with masses greater than 8 $M_\odot$ in the LMC (Whitney et al. 2008; Gruendl & Chu 2009). At the earliest stages of formation, YSOs are enshrouded by dust and gas. Their radiation is absorbed by the dust and gas, and subsequently reprocessed to output emission at far-IR wavelengths. *Herschel* Photoconductor Array Camera and Spectrometer (PACS) and Spectral and Photometric Imaging Receiver (SPIRE) data cover the far-IR wavelength range of 70 – 500 μm, allowing for the identification of the youngest and most-embedded YSO candidates. Seale et al. (2014) found 2,493 YSO candidates using *Spitzer* and *Herschel* photometry, 73% of which were not identified with previous studies which only used *Spitzer*.

The angular resolution of *Spitzer* and *Herschel* ranges from 1.7″ in the IRAC 3.6 μm band to 40.5″ in the SPIRE 500 μm band. Channel 1 MIRI/MRS observations have a FOV that is 3.2″ × 3.7″. Our MRS observations reveal that what appeared to be a single YSO in *Spitzer* and *Herschel* observations is actually a small cluster of YSOs in S1, S2, and E1. MRS observations of W1 reveal a single YSO.

We use the *Spitzer* and *Herschel* photometry from Gruendl & Chu (2009) and Seale et al. (2014) to fit spectral energy distribution (SED) models to get estimates of the total mass and luminosity of the clusters in E1, S1, and S2, and of the isolated YSO in W1. **The 'spbhmi' Robitaille (2017) SED model grid used in this work includes 10,000 model YSOs with a wide range of parameters: stellar radius ($0.1 - 100\,R_\odot$), stellar temperature (2000 – 30000 K), disk mask ($10^{-8} - 10^{-1}\,M_\odot$), outer disk radius (50 – 5000 AU), envelope density ($10^{-24} - 10^{-16}$ g cm^{-3}), envelope power-law (-2 to -1), cavity density($10^{-23} - 10^{-20}$ g cm^{-3}), and cavity opening angle ($0° - 60°$).** Figure 7 shows the Robitaille (2017) best-fit SED models fit to the observed mid-IR and far-IR data. **The *Spitzer* IRAC observations are in black circles, the *Spitzer* MIPS and *Herschel* observations are in black triangles fitted as upper limits. The beam size of *Spitzer* MIPS, *Herschel* PACS, and *Herschel* SPIRE observations range from 6″ – 35″ (Meixner et al. 2006, 2013). Mid- and far-IR emission from the central protostar and the surrounding dust will be unresolved by the MIPS, PACS, and SPIRE due to the beam size being much larger than the 1″ – 2″ beam size of IRAC (Meixner et al. 2006). Therefore, the mid- and far-IR photometry is fit as upper limits when we use the SED models. The best-fit models** for sources E1, S1, and S2 show a rise in flux toward mid-IR wavelengths, which is typical for YSOs. **The best-fit model for** source W1 is a more-evolved YSO as inferred from the SED: There is some IR emission seen with the bump around 100 μm, however the optical light from the star is also seen in the SED with the bump around 10 μm.

The mass of the clusters E1, S1, S2, and the isolated YSO Y1 in W1 determined by fitting the SEDs with Robitaille (2017) models are 18.3 ± 2.7, 25.4 ± 3.2, 15.7 ± 4.5, and 13.6 ± 1.6 $M_\odot$, respectively. The luminosity of E1, S1, S2, and W1 are $4.1 \pm 1.9 \times 10^4$, $1.2 \pm 0.5 \times 10^5$, $3.1 \pm 1.2 \times 10^4$, and $1.3 \pm 0.6 \times 10^4$ $L_\odot$, respectively. The effective temperatures are 17000 ± 6100, 19000 ± 5900, 17000 ± 7000, and 11000 ± 5500 K, respectively. S1 is the most massive cluster, with a luminosity one to two orders of magnitude higher than any of the other sources E1, S2, and **W1**. **Within a cluster, a single massive YSO typically dominates the overall luminosity (Looney et al. 2006). Therefore, we assume Y2 dominates in E1, Y4 dominates in S1, and Y9 dominates in S2. Y1 is an isolated YSO in W1.** With the addition of MRS observations, we are able to analyze each individual YSO in the *Spitzer*- and *Herschel*-identified clusters.

5. PRELIMINARY RESULTS OF SPECTRA

With the IRS onboard *Spitzer*, Seale et al. (2009) observed H72.97-69.39 (S1) and three other YSO candidates S2, E1, and W1. S1 and S2 have silicate absorption features and fine-structure emission lines, E1 has broad PAH emission and silicate absorption features, and W1 has PAH features but not silicate absorption. Silicate absorption features seen at 10 and 18 μm, as well as other ice absorption features which will be described in §5.5, are indicative of a young protostar embedded within its parental clump. As a YSO evolves, the UV photons from the central ionizing source lead to PAH and fine structure emission lines observed in its spectrum. The CC and CH stretching and bending modes of PAHs trace properties of the photoelectric effect and the heating/cooling of the ISM (Draine et al. 2007; Tielens 2008). The fine structure line emission is related to the hardness of the UV radiation and can be used to determine conditions of the shock-heated gas (Hollenbach et al. 1989). *Spitzer* IRS observations of S2 show silicate absorption features and no PAH or fine

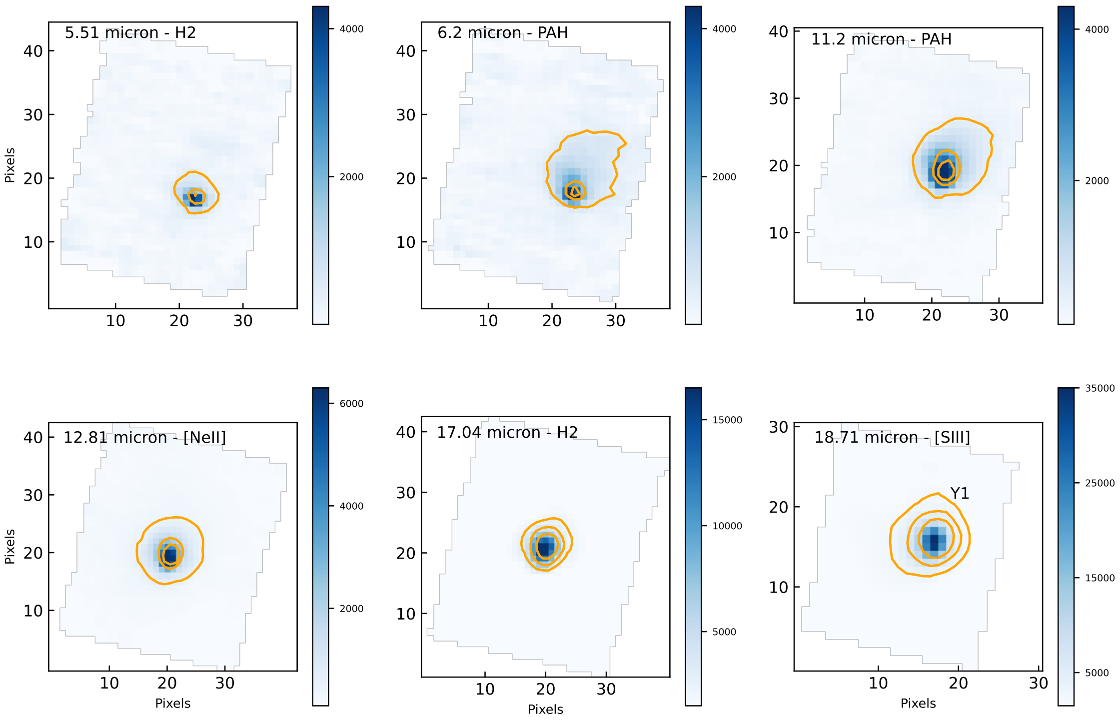

Figure 3. Slices of the IFU cube in N79W: The H_2 0-0 S7 emission at 5.51 μm (top left), PAH emission at 6.2 μm (top center), PAH emission at 11.2 μm (top right), [Ne II] emission at 12.81 μm (bottom left), H_2 0-0 S1 emission at 17.04 μm (bottom center), and [S III] emission at 18.71 μm (bottom right). We label this single YSO as 'Y1' in the bottom right panel. The contour levels for H_2 emission at 5.51 μm, PAH emission at 6.2 μm, PAH emission at 11.2 μm, and [Ne II] emission at 12.81 μm are 500, 2500, and 4500 MJy sr^{-1}. The contour levels for H_2 emission at 17.04 μm and [S III] emission at 18.71 μm are 2500, 5000, and 10000 MJy sr^{-1}.

structure emission, making this the youngest source in our MRS observations. The other three sources in this work have a combination of silicate absorption, PAH emission, and fine structure line emission.

The MRS spectra of Y1, Y2, Y3, Y4, Y6, and Y9 all show increasing flux towards mid-IR wavelengths, a **characteristic typical** of YSOs (Figure 2). Additionally, we see broad absorption lines, broad PAH emission lines, and narrow emission lines. The long-wavelength MRS sub-band 4C has a lower signal-to-noise (S/N) ratio, making line fitting from wavelengths 24.4 to 28.6 μm less reliable. Even in sub-bands 1A through 4B, the fluxes extracted from Gaussian fitting are dependent upon determining emission- and absorption-free ranges for continuum fitting and subtraction. Modeling the emission lines with `CLOUDY` and `PAHFIT` will be done in a later paper. In this work, we discuss the details of the various emission and absorption lines of **six out of the 11 total** YSOs from the N79 region of the LMC shown in Figures 8 – 13 and reported in Tables 1 – 6. **The five other YSOs in this sample have partial spectra. Additionally, the few emission lines they have are similar to one of the YSOs with a full MRS spectrum, implying these are not the dominating source within the cluster.**

5.1. *PAH Emission*

PAHs are essential to the balance between photoionization and recombination rates. Mid-IR observations of dusty sources (e.g., YSOs, H II regions, planetary nebulae, reflection nebulae, **and** asymptotic giant branch stars) often show PAH emission at 6.2, 7.7, 8.6, 11.2, 12.7, and 16.4 μm (Hony et al. 2001; Peeters et al. 2002; Shannon et al. 2016). The PAH features in the 5 – 10 μm region originate from the pure CC stretching mode as well as the CH in-plane bending mode (Joblin et al. 1996; Hony et al. 2001). The 10 – 15 μm PAH features are due to the out-of-plane bending vibrations of aromatic H atoms (Hony et al. 2001). **The 7.7 μm emission feature originates from positively-charged grains, whereas the 11.2 μm emission is from neutral grains (Hony et al. 2001). The PAH$_{11.2}$/PAH$_{7.7}$ ratio is sensitive to the fraction of ionized to neutral PAHs (Draine & Li 2001).** The 15 – 20 μm region is because of the CCC modes of PAHs (Smith et al. 2007). In addition to the above six PAH emission lines, we also observe the **faint and positively-charged** 11 μm feature for three YSOs in N79.

The 6.2 μm PAH feature is seen in the spectra of Y1 located in W1, Y2 located in E1, Y6 located in SSC region S1, and Y9 located in S2. The 6.2 μm emission for sources Y6 and Y9 have a red tail which can be seen in Figures 12 and 13. The peak position of the 6.2 μm PAH feature for Y6 is 6.239 μm whereas for the other three sources the peak position ranges from 6.225 - 6.227 μm, slightly shorter in wavelength. Additionally, source Y6 has a full width half maximum (FWHM) of 0.123 μm, larger than the FWHM of the 6.2 μm for Y1, Y2, and Y9 by 20%. Peeters et al. (2002) observe a similar asymmetric red tail and larger FWHM for the PAH emission whose peak positions are greater than 6.23 μm for 57 different dusty sources, including YSOs, planetary nebulae, and other galaxies. They attribute the observed asymmetry in the 6.2 μm emission line to a combination of PAH stretching and bending modes, one with emission at 6.2 μm and another with emission at 6.3 μm.

The 7.7 μm PAH feature is seen as a double emission line for sources Y1 and Y2, where there is a peak around 7.6 μm, arising from small grains, and another peak around 7.8 μm, arising from large grains. The 7.6 μm feature is the dominant emission with a flux 10% greater than the 7.8 μm feature in Y1, and 40% greater than the 7.8 μm feature in Y2. Sources Y6 and Y9 also emit the 7.7 μm PAH feature, however there is no secondary emission around 7.8 μm.

The 8.6 μm and much weaker 11.0 μm PAH emission lines are present in Y1, Y2, and Y9. The 8.6 μm line is 63, 13, and 15 times stronger than the 11.0 μm line for sources Y1, Y2, and Y9, respectively. The charged state of the ionized PAHs which emit in the 5 – 10 μm region also lead to the 11.0 μm emission (Hudgins et al. 2004). Peeters et al. (2017) find a correlation between the 8.6 μm and 11.0 μm emission. Their observations show that the 8.6 μm emission from the CH in-plane bending mode and the 11.0 μm emission from the out-of-plane bending mode of the H atom are closer to the central illuminating source NGC 2023. There also is a close correlation between the 7.6 μm and 11.0 μm PAHs (Peeters et al. 2017). We find that YSOs with both the 8.6 μm and 11.0 μm emission lines also have 7.7 μm emission, indicating a correlation of similar origin for the three different PAH emission lines.

Every YSO, except for Y4 located in the central ionizing source in H72.97-69.39, **exhibits** the 11.2 μm PAH emission line. Y1, Y2, and Y9 have the 12.7 μm and 16.4 μm PAH features. Further away from the central

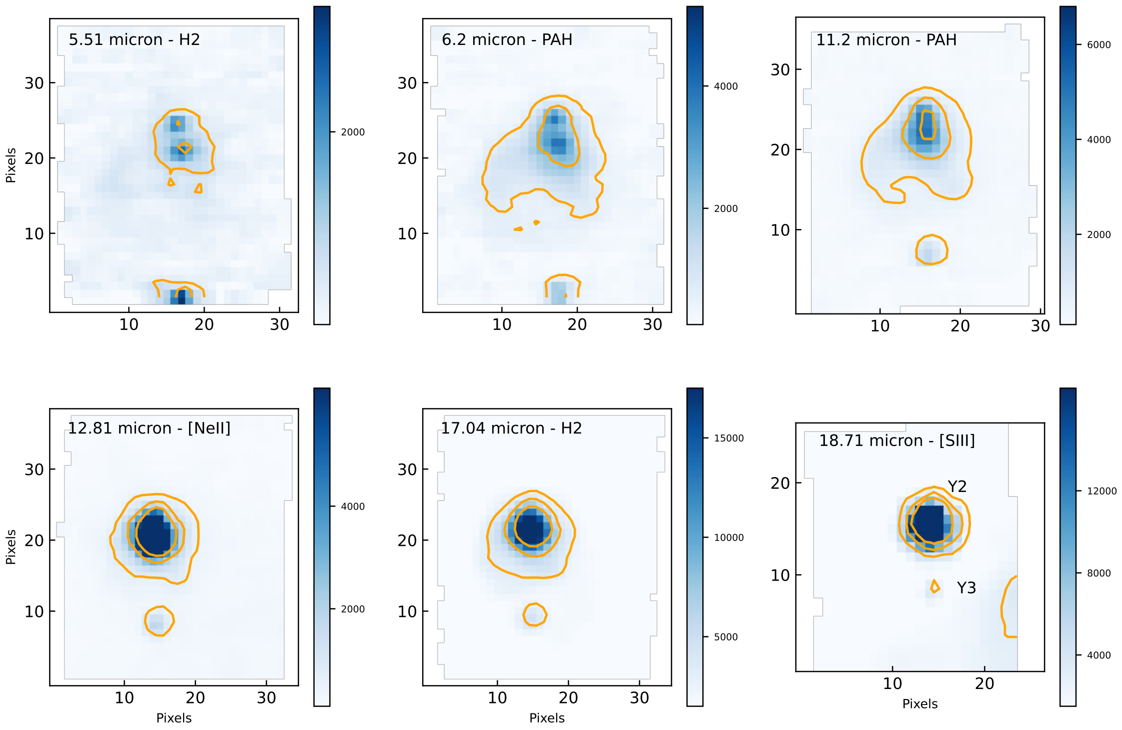

Figure 4. Slices of the IFU cube in N79E: The H_2 0-0 S7 emission at 5.51 μm (top left), PAH emission at 6.2 μm (top center), PAH emission at 11.2 μm (top right), [Ne II] emission at 12.81 μm (bottom left), H_2 0-0 S1 emission at 17.04 μm (bottom center), and [S III] emission at 18.71 μm (bottom right). We label the two sources within the MRS FOV as 'Y2' and 'Y3' in the bottom right panel. The contour levels for H_2 emission at 5.51 μm, PAH emission at 6.2 μm, PAH emission at 11.2 μm, and [Ne II] emission at 12.81 μm are 600, 2000, and 4500 MJy sr^{-1}. The contour levels for H_2 emission at 17.04 μm and [S III] emission at 18.71 μm are 3000, 6000, and 12000 MJy sr^{-1}.

ionizing source are the PAHs which give rise to the 7.7 μm emission line, more specifically the large grains which emit at 7.8 μm (Bauschlicher et al. 2008). With increasing proximity to the central ionizing source, these PAHs which emit at 7.8 μm break down into smaller grains which leads to the 11.2 μm emission. These PAHs are further broken down closer to the central ionizing source and emit at 12.7 μm and 16.4 μm. The 6.2, small grain 7.7, 8.6, and 11 μm PAH emission features occur closest to the central YSO.

Both shocks and UV radiation can enhance certain PAH emission lines by dissociating large grains, but they can also destroy the PAH molecules (Hony et al. 2001; O'Halloran et al. 2006). **The mass of the cluster S1 (including source Y4) is 25.4 $M_\odot$, and the luminosity is 1.2×10^5 $L_\odot$.** This cluster is an order of magnitude more luminous than the other clusters in this work, with Y4 most likely dominating the SED. Y4 has no PAH emission lines because of the intense ionizing radiation of this YSO **destroying PAH molecules**.

5.2. *Molecular Hydrogen Lines*

H_2 emission can be the result of shock heating of the molecular gas by outflows from the central protostar, or UV heating of nearby gas to a few hundred degrees Kelvin by the massive star. We find several H_2 rotational lines in Y1, Y2, Y3, Y4, Y6, and Y9. The three H_2 emission lines common to all six YSOs in this work are the H_2 0-0 S4 line at 8.03 μm, H_2 0-0 S3 line at 9.67 μm, and H_2 0-0 S1 line at 17.03 μm. We show the IFU slices at 5.51 μm (H_2 0-0 S7) and 17.03 μm in Figures 3 – 6. The 17.03 μm emission is stronger than that at 5.51 μm **indicating that** these are young and deeply-embedded YSOs with a steep rise in their SED toward mid-IR and far-IR wavelengths. Furthermore, the longer wavelength slices reveal additional embedded YSOs. This is especially noticeable for region S1 shown in Figure 5 where the 5.51 μm slice has two YSOs, whereas there are five YSOs in the 17.03 μm slice. Previous observations of reflection nebula NGC 2023 and the Orion Bar show the H_2 emission to trace PDR fronts (Peeters et al. 2017; Knight et al. 2021). Future analysis will use `PAHFIT` and `CLOUDY` modeling to derive gas properties based on the PAH emission lines and narrow fine structure emission lines. Properties such as extinction, shock excitation, temperature, density, and wind velocity will be calculated using line ratios (Morisset et al. 2002, 2004; Simpson et al. 2012; Stock et al. 2013; Lambert-Huyghe et al. 2022).

5.3. *Fine Structure Emission*

Fine structure emission is often seen in YSOs which also exhibit PAH emission, indicating that the central illuminating source is emitting UV radiation. Neon, sulfur, and argon lines have previously been observed in W1, E1, S1, and S2 with *Spitzer* IRS (Seale et al. 2009). In PDRs, the UV photons from the central star are ionizing atomic species with ionization potential 13.6 eV and below, (i.e., [Fe I], [Fe II], [Si I]). Shocks from winds and jets can heat up the gas to 10^5 K (Draine & McKee 1993; Hollenbach 1997). These strong shocks with velocities greater than 70 km s^{-1} result in [Ni II] 6.6, [Ar II] 6.9, [Ne II] 12.8, [Ar III] 8.9 and 21.8, and [Fe II] 26 μm emission lines which need high **ionization energy** (> 21 eV).

5.3.1. *Neon Fine Structure Line Emission*

The presence of [Ne II] and [Ne III], which requires **ionization energy** > 41 eV, means there are high-energy UV photons either from the central star or high-velocity shocks. YSOs Y1, Y2, Y3, Y4, and Y6 have both the [Ne II] 12.8 μm and [Ne III] 15.5 μm lines. YSO Y9 only has the [Ne II] 12.8 μm line. The [Ne II] / H_2 S(1) ratio (often used to infer shock velocity) for sources Y1, Y2, Y3, Y4, Y6, and Y9 are 15.4, 38.9, 0.5, 97.4, 38.8, and 5.1, respectively. **We use the Hollenbach et al. (1989) shock models of high-velocity ($v = 40 - 150$ km s^{-1}) jump shocks where gas is heated to temperatures as high as 10^5 K in a timescale shorter than the characteristic cooling time. At low densities ($n = 10^3 - 10^5$ cm^{-3}), hydrogen recombination lines, [Fe II] 5.3 μm, [Ne II] 12.8 μm, [Fe II] 26.3 μm are predicted from the models. When densities are $n = 10^5 - 10^7$ cm^{-3}, there is an increase in [Cl I] 11.3 μm, and [Fe I] 24 μm.** Assuming a molecular gas density of $n = 10^4$ – 10^5 cm^{-3} and using the Hollenbach et al. (1989) shock models, the shock velocities associated with the [Ne II] emission are 140, 120, 50, 100, 120, and 90 km s^{-1} for Y1, Y2, Y3, Y4, Y6, and Y9, respectively. A more detailed constraint using multiple fine structure line ratios will be presented in a later paper.

For shock velocities 30 – 40 km s^{-1}, Hollenbach et al. (1989) predict H_2 S(1), H_2 S(2), H_2 S(3), as well as the [Fe II] 26 μm to be stronger than the [Ne II] line by one to three orders of magnitude. However, we observe the [Ne II] line to be stronger in every source except for Y3, implying shock velocities >70 km s^{-1} (Hollenbach et al. 1989). Y3 is the youngest protostar in this study, with deep absorption lines implying this source is younger

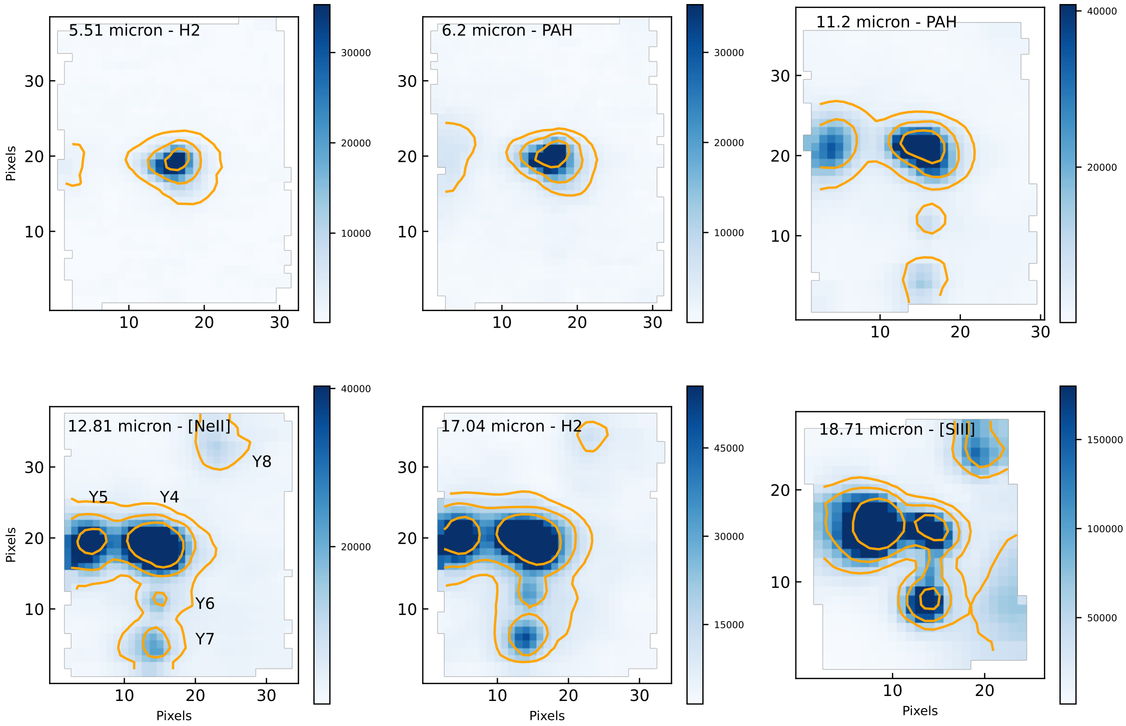

Figure 5. Slices of the IFU cube in N79S1: The H_2 emission at 5.51 0-0 S7 μm (top left), PAH emission at 6.2 μm (top center), PAH emission at 11.2 μm (top right), [Ne II] emission at 12.81 μm (bottom left), H_2 0-0 S1 emission at 17.04 μm (bottom center), and [S III] emission at 18.71 μm (bottom right). We label the five sources within the MRS FOV as 'Y4', 'Y5', 'Y6', 'Y7', and 'Y8' in the bottom right panel. The contour levels for H_2 emission at 5.51 μm are 2000, 10000, and 35000 MJy sr^{-1}. The contour levels for PAH emission at 6.2 μm are 4000, 10000, 35000 MJy sr^{-1}. The contour levels for PAH emission at 11.2 μm and [Ne II] emission at 12.81 μm are 5000, 15000, and 45000 MJy sr^{-1}. The contour levels for H_2 emission at 17.04 μm are 9000, 20000, and 55000 MJy sr^{-1}. The contour levels for [S III] emission at 18.71 μm are 35000, 80000, and 230000 MJy sr^{-1}.

than 10,000 years old. The lack of multiple different ionization lines and the low shock velocity inferred from the Hollenbach et al. (1989) models suggests that Y3 is still very embedded: The UV radiation from the central star has not yet begun to ionize the surrounding gas and the accretion rate is lower in comparison to the other five YSOs in this work. Hollenbach & Gorti (2009) find shocks from protostellar winds can explain the observed [Ne II] emission, especially when the mass accretion rate (which is proportional to the protostellar wind mass loss rate) is higher than 10^{-8} $M_\odot$ yr^{-1}. However, they also find that low-mass protostars with low accretion rates are associated with [Ne II] due to UV and X-ray radiation from nearby high-mass stars photoexciting the gas (Hollenbach & Gorti 2009).

5.3.2. *Sulfur and Iron Lines in Spectra of Protostars*

If high shock velocities are the origin of the observed line emission, the [Fe I] line at 24 μm and [S I] line at 25.3 μm should be detected, with the [S I] line being the stronger of the two (Hollenbach et al. 1989). With low-velocity shocks, H_2 emission is particularly strong and atomic lines are expected to be weak (Kaufman & Neufeld 1996). The YSOs in this work likely have a mix of high- and low-velocity shocks since we observe strong fine structure atomic lines as well as multiple H_2 lines. [S I], [Fe I], and [Fe II] lines can be used to determine if slow- or fast-velocity shocks are dominating the region (Hollenbach et al. 1989).

5.3.3. *Detection of [Cl II]*

The [Cl II] fine structure emission line at 14.37 μm is observed for sources Y1, Y2, Y4, Y6, and Y9. The offset velocity of the [Cl II] line is 7.9, 4.5, 13.4, 26.4, and 10.9 km s^{-1} for sources Y1, Y2, Y4, Y6, and Y9, respectively. The [Cl II] line has an ionized potential of 13 eV and could originate from shocks where the ionized gas is heated up to 10^5 K (Hollenbach et al. 1989). Collimated jets associated with Herbig-Haro (HH) objects HH529 and HH204 have been observed in the Orion Nebula (Méndez-Delgado et al. 2021b,a). Line emission from [Cl II], [Cl III], and [Cl IV] has been observed with both HH sources with velocity offsets ranging from 11 km s^{-1} to 36 km s^{-1} (Méndez-Delgado et al. 2021b,a), similar to the velocity offset we observe with the [Cl II] emission line associated with YSOs in N79. Low-velocity jets and bow shocks <30 km s^{-1} could be one possible origin for the observed [Cl II] in N79 YSOs.

5.4. *H I Emission Line*

MRS observations reveal, for the first time, several mid-IR hydrogen recombination lines in the spectra of extra-galactic YSOs in N79. Hydrogen recombination lines can be used to estimate the accretion rate. Alcalá et al. (2014) use Very Large Telescope (VLT) X-shooter to observe the Brackett, Balmer, and Paschen hydrogen recombination lines to **derive** accretion rates of $2 \times 10^{-12} - 2 \times 10^{-8}$ $M_\odot$ yr^{-1} for low-mass YSOs in the mass range 0.3 – 1.2 $M_\odot$. Deeply-embedded sources like the YSOs in this work require detection of mid-IR hydrogen recombination lines. We find Y1, Y2, Y4, and Y6 to have both the H I (9-7) emission at 11.31 μm and the Humphreys α H I (7-6) emission at 12.37 μm. Y9 has only the H I (7-6) emission.

Rigliaco et al. (2015) used *Spitzer* IRS observations of 114 T-tauri stars with disks to find a correlation between the H I (7-6) emission and the accretion luminosity:

$$\log \frac{L_{HI(7-6)}}{L_\odot} = (0.48 \pm 0.09) \times \log \frac{L_{acc}}{L_\odot} - (4.68 \pm 0.10). \tag{1}$$

The factor of 0.48 from Rigliaco et al. (2015) sets a nearly quadratic dependence between the line and accretion luminosity. This strong dependence is at odds with the nearly linear relation commonly reported by other studies for different lines (see e.g. Table 4 of Alcalá et al. 2014) and could be driven by a few scattered points. We present our calculations both with this factor and setting it to 1.0. The H I (7-6) line luminosity of Y1, Y2, Y4, Y6, and Y9 are 0.10 ± 0.03, 0.52 ± 0.05, 5.59 ± 0.45, 0.79 ± 0.45, **and** 0.07 ± 0.01 $L_\odot$**, respectively. In turn, the accretion luminosity calculated using the above equation for each source has a range between** $1.02 \times 10^6 - 9.93 \times 10^9$, $2.68 \times 10^7 - 4.56 \times 10^{11}$, $1.92 \times 10^9 - 1.82 \times 10^{14}$, $8.85 \times 10^6 - 3.84 \times 10^{12}$, **and** 6.83×10^5 $L_\odot$ $- 2.55 \times 10^9$**, respectively when using the 0.48 factor. Without the 0.48 factor, the accretion luminosity is** $2.65 \times 10^3 - 7.92 \times 10^3$, $1.71 \times 10^4 - 3.52 \times 10^4$, $1.95 \times 10^5 - 3.64 \times 10^5$, $9.11 \times 10^3 - 8.09 \times 10^4$, **and** 2.12×10^3 $L_\odot$ $- 4.66 \times 10^3$**, respectively. The range calculated takes into account the error in the fits from Rigliaco et al. (2015) as well as the error in measured flux.**

Following Gullbring et al. (1998) we estimate the mass accretion $\dot{M}_{acc}$ **balancing the gravitational energy lost by the material falling from the inner disk magnetospheric radius** R_m **to stellar radius** R_{star} **with the accretion luminosity**

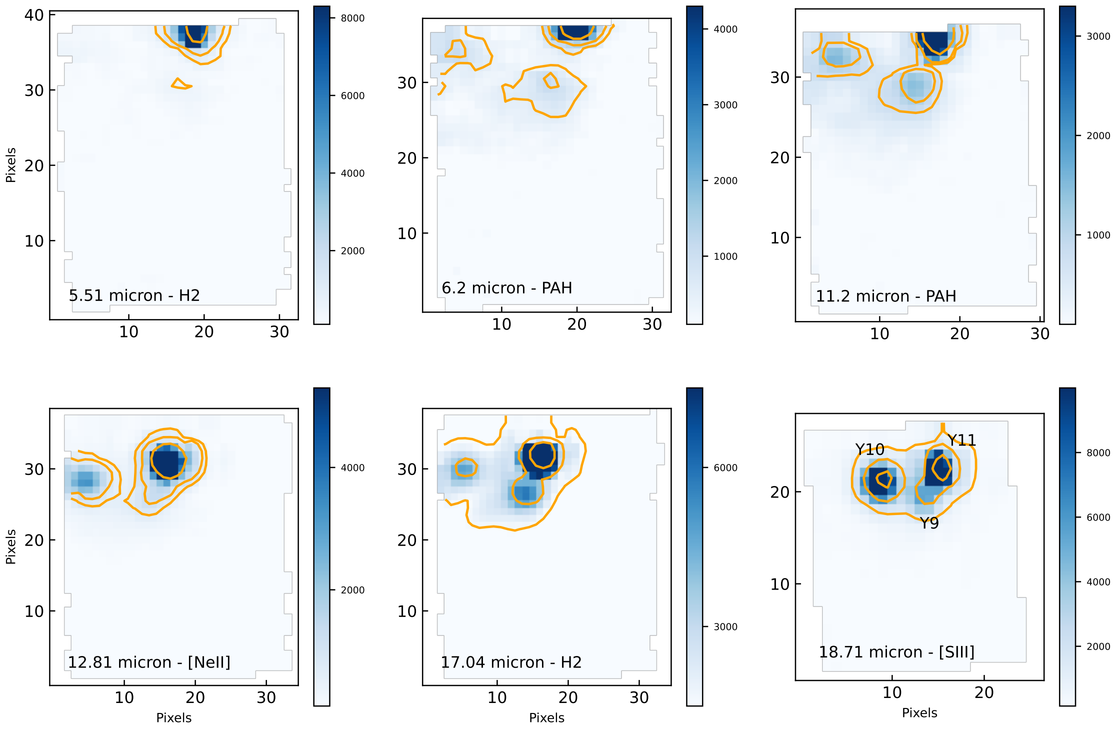

Figure 6. Slices of the IFU cube in N79S2: The H_2 0-0 S7 emission at 5.51 μm (top left), PAH emission at 6.2 μm (top center), PAH emission at 11.2 μm (top right), [Ne II] emission at 12.81 μm (bottom left), H_2 0-0 S1 emission at 17.04 μm (bottom center), and [S III] emission at 18.71 μm (bottom right). We label the three sources within the MRS FOV as 'Y9', 'Y10', and 'Y11' in the bottom right panel. The contour levels for H_2 emission at 5.51 μm are 500, 1000, and 8000 MJy sr^{-1}. The contour levels for the PAH emission at 6.2 μm are 500, 1000, and 4000 MJy sr^{-1}. The contour levels for the PAH emission at 11.2 μm are 700, 1000, and 3000 MJy sr^{-1}. The contour levels for the [Ne II] emission at 12.81 μm are 600, 1000, and 4000 MJy sr^{-1}. The contour levels for H_2 emission at 17.04 μm are 1500, 4000, and 15000 MJy sr^{-1}. The contour levels for the [S III] emission at 18.71 μm are 1000, 4000, and 15000 MJy sr^{-1}.

L_{acc} emitted by the shock at the stellar surface:

$$\dot{\mathrm{M}}_{\mathrm{acc}} \simeq \frac{\mathrm{L}_{\mathrm{acc}}\mathrm{R}_{\mathrm{star}}}{\mathrm{GM}_{\mathrm{star}}}\left(1-\frac{R_*}{R_m}\right). \quad (2)$$

The term in parenthesis is of the order unity and for simplicity we set it equal to 1. We then use the stellar radius and stellar mass derived by fitting Robitaille (2017) SED models to calculate the mass accretion of Y1, Y2, Y4, and Y9. **In using the parameters output from the SED modeling, we are assuming that a single YSO in E1, S1, and S2 is dominating the SED. Including the 0.48 factor from Rigliaco et al. (2015), the mass accretion rate of Y1, Y2, Y4, and Y9 range between 1.18×10^{-1} – 1.16×10^{3}, 1.23×10^{0} – 2.09×10^{4}, 9.94×10^{1} – 9.44×10^{6}, 3.93×10^{-2} – 1.46×10^{2} $M_\odot$ yr^{-1}. These values are very high and imply that the star formation process is occurring on extremely short timescales, a few years or a few hundred years. Instead, ignoring the 0.48 factor in Equation 1, the mass accretion rate of Y1, Y2, Y4, and Y9 range between 3.09×10^{-4} – 9.23×10^{-4}, 7.83×10^{-4} – 1.61×10^{-3}, 1.01×10^{-2} – 1.89×10^{-2}, 1.22×10^{-4} – 2.69×10^{-4} $M_\odot$ yr^{-1}. These values are similar to the upper-limit of typical rates which have been measured for YSOs in the Milky Way, 10^{-4} $M_\odot$ yr^{-1} (Rigliaco et al. 2015). On the other hand, the mass accretion rate of Y1, about 0.01 – 0.02 $M_\odot$ yr^{-1}, is two orders of magnitude higher than low-mass YSOs in the Milky Way, and alludes to the extreme nature of this particular YSO at the center of SSC candidate H72.97-69.39.**

Examining the disk mass parameter output from the Robitaille (2017) SED models and assuming a typical formation timescale of 10^5 yr^{-1}, the mass accretion rate (disk mass divided by the formation timescale) is $1.83 \pm 0.34 \times 10^{-7}$, $7.91 \pm 0.19 \times 10^{-8}$, $9.32 \pm 3.46 \times 10^{-8}$, and $7.06 \pm 0.18 \times 10^{-8}$ for Y1, Y2, Y4, and Y9, respectively. Alternatively, Nayak et al. (2019) study the ^{13}CO molecular gas outflows from Y4 in H72.97-69.39 and calculate the accretion rate based on the size of the red- and blue-shifted accretion lobes to be 8× 10^{-4} $M_\odot$ yr^{-1}. Two caveats to note are that 1) high-mass YSOs in the low-metallicity environment of the LMC likely have a different relation between the H I (7-6) line luminosity and the accretion luminosity, which was based on Hα observations of low-mass T-Tauri stars in the Milky Way (Rigliaco et al. 2015), and 2) the excess mass accretion rate we measure in the spectra of Y4 could be from strong winds or UV radiation also ionizing H I (7-6).

Hydrogen recombination line ratios can be used to determine conditions of the gas such as temperature and density. In this work, the H I (9-7) / H I (7-6) line ratios are 0.242, 0.164, 0.123, and 0.192 for Y1, Y2, Y4, and Y6, respectively. Kwan & Fischer (2011) created a model grid of expected hydrogen recombination line ratios for low-mass YSOs based on input temperature (5000 – 20000 K), hydrogen density (10^8 – $10^{12.4}$ cm^{-3}), ionization rate, and velocity gradient transverse to the radial direction (the ratio of the turbulent/thermal linewidth). Their predicted H I (9-7) / H I (7-6) line ratios ranged from 0.3 – 2.1, higher than the observed line ratios in this work which range from 0.12 – 0.24. **An increase in dl/dv, the ratio of the turbulent/thermal linewidth, leads to an increase in the line optical depth, τ (equation 1 in Kwan & Fischer 2011), which is one of the parameters in their modelings. Kwan & Fischer (2011) assume the velocity gradient dl/dv is not large and the model results do not vary much on the gradient. Massive stars whose turbulent velocity from winds and radiation is larger than that of low-mass stars would have very different dl/dv than what was modeled, and therefore could be the reason we find the H I (9-7) / H I (7-6) line ratios to be smaller than the predicted ratios from Kwan & Fischer (2011).**

Hollenbach & Gorti (2009) find the ratio of H I (7-6) to the [Ne II] fine structure line to theoretically be 0.008 due to extreme UV- and X-ray-illuminated shocks. The observed ratios in this work range from 0.11 for Y4 to 0.04 for Y1, Y2, Y5, and Y6. The observed ratios are higher than the theoretical ratios which means the origin of the hydrogen recombination line must be from regions where the density is higher than the critical density of [Ne II]. Hollenbach & Gorti (2009) suggest an alternate scenario where the observed H I lines in high-mass protostars in N79 could arise from shocks due to high-velocity winds. Hollenbach & Gorti (2009) find winds with velocities > 100 km s^{-1} that occur close to the origin of the central source (< 1 AU) leading to densities where H I (7-6) emission is enhanced, but the [Ne II] emission is suppressed. **This excess H I (7-6) emission would also explain the high mass accretion rates calculated, since the measured emission would be from shocks and winds in addition**

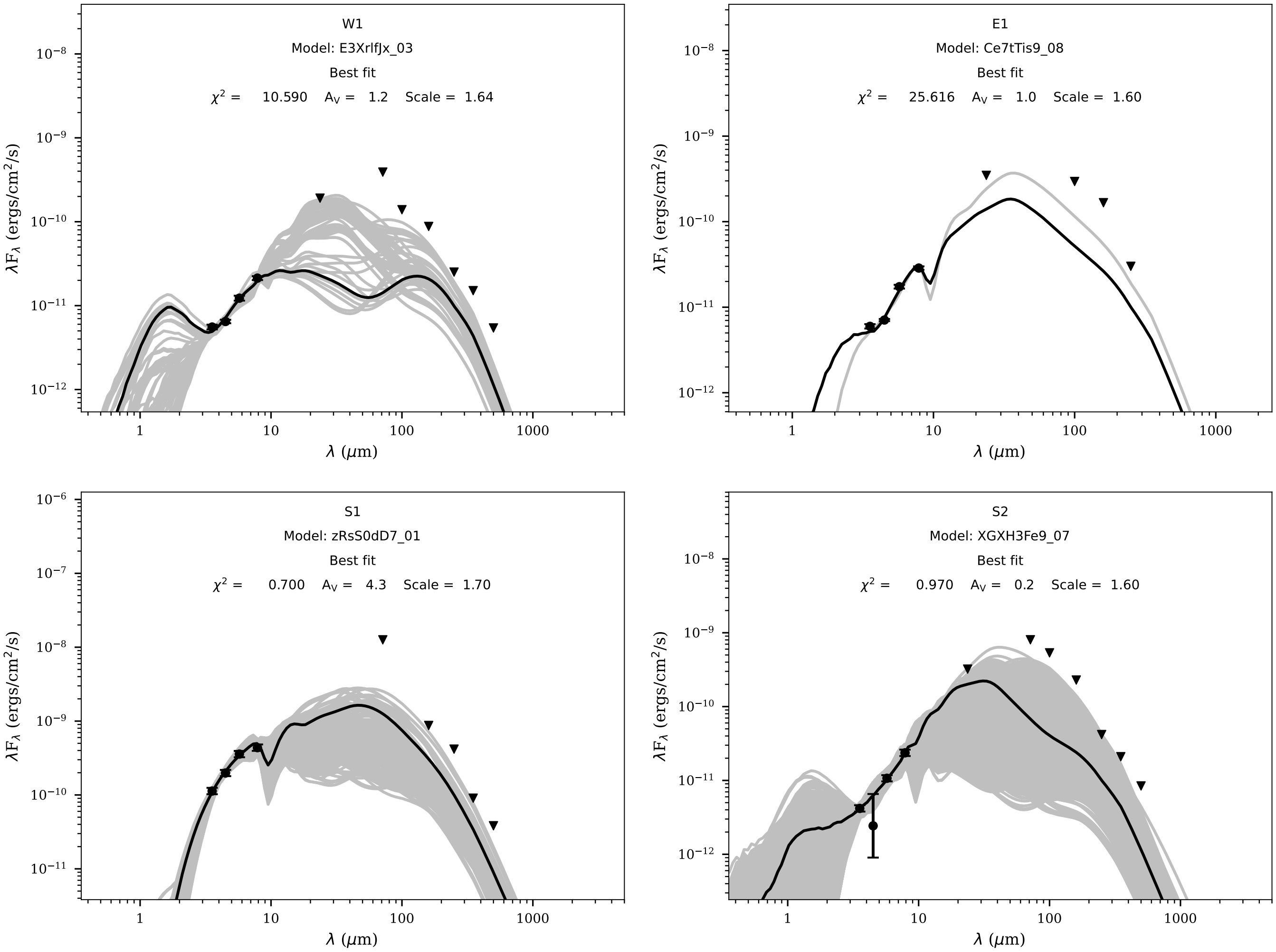

Figure 7. Robitaille (2017) SED models fit to the *Spitzer* and *Herschel* photometry for W1, E1, S1, and S2. The black circles are the *Spitzer* IRAC photometry, the black triangles are the *Spitzer* MIPS, *Herschel* PACS, and *Herschel* SPIRE photometry fitted as upper limits. **The black dots are the fitted data points, the black triangles are upper limits, the black line is the best-fit model, and the gray lines are are models which have χ^2<3 relative to the best-fit model.**

to accretion. Massive YSOs have previously been observed to have high-velocity winds: S106-IR has an ionized wind with a velocity of 340 km s^{-1} (Drew et al. 1993), and W51 IRS2 is a 60 $M_\odot$ O star with a 200 $M_\odot$ molecular outflow and wind velocities of 100 km s^{-1} inferred from the [Ne II] emission line (Lacy et al. 2007; Zapata et al. 2009). Given that these YSOs in N79 are very massive ($11 - 25$ $M_\odot$) and extremely luminous ($6.8 \times 10^3 - 1.3 \times 10^5$ $L_\odot$), outflows with velocities > 100 km s^{-1} are a likely scenario. **Such conditions in N79 would explain why the observed H I (7-6) to [Ne II] ratio is higher than theoretical models.**

5.4.1. *The Central Illuminating Source Y4 in H72.97-69.39*

MRS observations of H72.97-69.39 show five sources within the FOV (Figure 5). Figure 2 shows the spectra of Y5, Y7, and Y8 which are not complete, but still show similar emission line features to Y4 and Y6 in channels 3 and 4. The *Spitzer* IRS spectrum of S1, shown in red in Figure 2, resembles the MRS spectrum of Y4. This is the more-luminous source and is likely dominating the SED of the small cluster, with Y6 as the second-most dominant source. ALMA observations of H72.97-69.39 reveal two filaments colliding, with Y4 located in the center (Nayak et al. 2019). Figure 14 shows the blue- and red-shifted outflows observed with ^{13}CO on the MRS channel 3 slice of H72.97-69.39. Nayak et al. (2019) find an outflow rate of 0.008 $M_\odot$ yr^{-1} associated with the central protostar inferred from the red-shifted outflow lobe, four times higher than outflow rates of massive YSOs in the Milky Way (Beltrán et al. 2011). Commonly found to trace hot molecular cores and the cavity of outflowing jets, SO is a useful diagnostic of shocked gas (Esplugues et al. 2013; Codella et al. 2014). ALMA SO observations trace gas densities of 10^6 cm^{-3} which are offset from the outflow axis by 90°. Further ALMA observations with spectral resolution higher than that used by Nayak et al. (2019) is necessary to determine the kinematic structure of SO. It is possible the high-velocity winds > 100 km s^{-1} that cause the hydrogen recombination line H I (7-6) emission also lead to the observed SO emission. The wind could be compressing the gas to 10^6 cm^{-3} in the immediate vicinity of Y4, leading to a lower [Ne II] emission, higher H I (7-6) emission, and the observed SO emission (Hollenbach & Gorti 2009; Nayak et al. 2019).

Reiter et al. (2019) use the Folded-Port Infrared Echellette (FIRE; Simcoe et al. 2013) on the 6.5 m Magellan/Baade telescope to observe the near-IR spectrum of H72.97-69.39 (with Y4 likely being the dominating YSO). They find the H_2/Brγ ratio (i.e., the ratio of collisionally excited to photoexcited gas) is 0.01. Additionally, Reiter et al. (2019) find the region around H72.97-69.39 is likely not shock-excited based on the low [Fe II] 1.64 μm/Paβ **and [Fe II] 1.64 μm/Brγ ratios of 0.02 and 0.11, respectively**. Both Brγ and Paβ are **likely** photoexicted **by** the far-UV radiation within H II regions (Mouri et al. 2000). The region around Y4 and Y6 is possibly PDR dominated with still some effects from shocks originating in protostellar jets, outflows, **and accretion**.

5.5. *Absorption Features in MRS Spectra*

We detect a mixture of solid- and gas-phase absorption features in the MRS spectra of massive YSOs in N79. The solid-phase ice absorption feature **of** CO_2 is indicative that the protostar is very young and deeply-embedded within its parental GMC. Gas-phase absorption features **of** HCN and CO_2 trace warm and dense gas (Boonman et al. 2003a,b). Boonman et al. (2003b) observe the compact IR source Orion-IRc2 and find HCN to be radiatively excited, while CO_2 originates in the $150 - 200$ K warm component of the shocked gas. We qualitatively discuss here the absorption features seen in the spectra of Y1, Y3, Y4, Y6, and Y9 (YSO Y2 has no absorption features).

NH_3: There is a narrow absorption line detected near 6.12 μm in the spectra of Y1 and Y4 which we tentatively assign to NH_3. This feature is typically **observed as** a broad absorption feature around 6 μm, along with the broad absorption feature due to the H_2O bending mode in the same wavelength range. Due to **this peculiarity**, this **narrow absorption line** at 6.12 μm could potentially be an unidentified line species.

C_2H_5OH: We have labeled the 7.23 μm absorption feature observed in Y1 as absorption from C_2H_5OH, which could be mixed with HCOOH. The CH/OH deformation mode of HCOOH and the CH_3 symmetric deformation mode of C_2H_5OH could both be contributing to this feature (Schutte et al. 1999; Öberg et al. 2007). The C_2H_5OH and HCOOH feature has previously been observed with *Spitzer* IRS as well as Infrared Space Observatory (ISO) for YSOs in the Perseus, Taurus, Serpens, and Corona Australis molecular cloud complexes (Boogert et al. 2008). Yang et al. (2022) also see this absorption feature in the MRS spectra of IRAS 15398-3359, a young protostar with shell-like outflows.

HCN and CO_2 gas-phase absorption: The HCN gas-phase absorption line at 14.05 μm is detected in Y6, while the CO_2 gas-phase absorption line at 14.97 μm

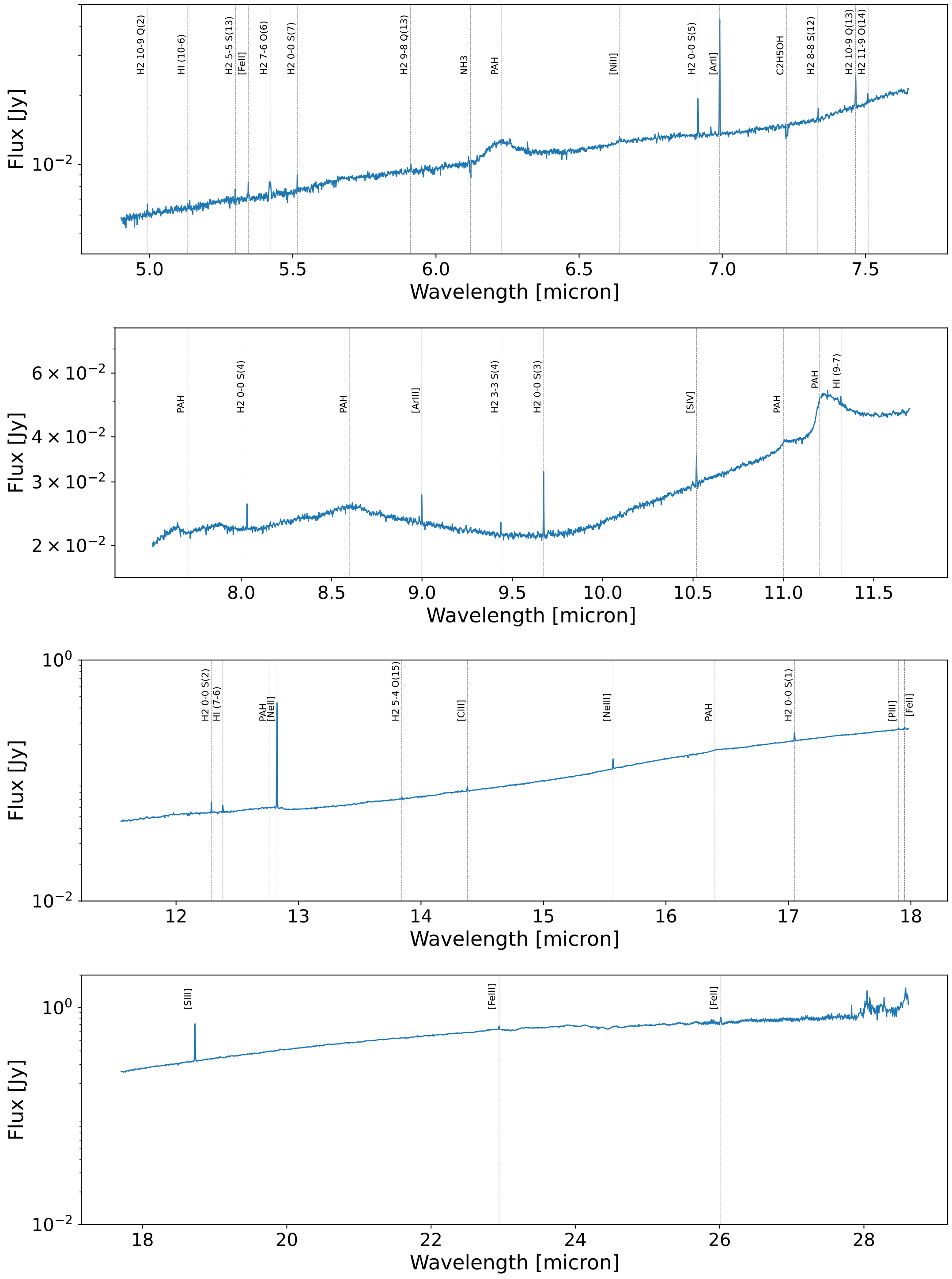

Figure 8. Spectra taken in channels 1-4 of Source Y1 in N79 West. Full line list is given in Table 1.

is detected in Y9. HCN and CO_2 gas-phase absorption lines have previously been found to originate either in disks around protostars or from winds emanating from disks (Lahuis et al. 2006). The HCN absorption in Y6 is blue-shifted. This deviation from Keplerian rotation in the plane of the disk could imply the presence of stellar winds or a binary system. Rodgers & Charnley (2003) model early-stage protostars to find that HCN and CO_2 gas-phase absorption features cannot be explained by evaporation of ices alone, but rather additional high-temperature gas in the inner envelope region around a YSO is necessary. **While** evidence for a disk around an O-star remains elusive, the gas surrounding protostars Y6 and Y9 could be heated to high temperatures (>100 K) from winds, shocks, and radiation from the star, increasing the abundance of HCN and CO_2.

CO_2 doublet: Sources Y3 and Y9 show the broad CO_2 absorption feature around 15.2 μm, which is from the bending mode of CO_2. The CO_2 doublet feature with one peak at 15.1 μm and another peak at 15.25 μm can be seen in the spectra in Figures 10 and 13. The CO_2 absorption feature in Y3 is much deeper than in Y9. The CO_2 is likely formed in a H_2O-rich environment where the star heats up the CO, CO_2, and H_2O molecules to also form CH_3OH, which can be seen with the broad shoulder towards 15.4 μm in the spectra of Y3 (Gerakines et al. 1999). **A three-Gaussian fit allows us to discern the** CO_2 + CO absorption at 15.1 μm, the CO_2 + H_2O at 15.25 μm, and the CH_3OH broad emission feature at 15.4 μm for Y3 **(shown in figure 18)**. There are two reasons the CO_2 ice-absorption feature in Y9 is not as strong as the one seen in Y3 and the broad CH_3OH emission is not seen in Y9: Either Y9 is a more evolved protostar and therefore the ice-absorption features are not as predominant in the spectrum, and/or Y9 is a lower-mass protostar than Y3 since lower-mass YSOs are observed to show a weaker 15.4 μm broad shoulder (Pontoppidan et al. 2008).

5.5.1. *The Young and Deeply-Embedded YSO Candidate in N79 East*

In addition to the broad CO_2 doublet absorption feature, the spectrum of Y3 also shows CH_4, NH_3, CH_3OH, and CH_3OCHO absorption features at 7.7, 8.9, 9.7, and 13.02 μm, respectively. We show some of these absorption features in Figures 15 - 18. Modeling CH_4 has shown that these molecules rapidly form on cool grains through successive hydrogenation of atomic carbon (Tielens & Hagen 1982). CH_4 abundances have been observed to be constant in a variety of low- and high-mass YSOs, whereas CH_3OH abundances vary by up to a factor of 10 depending on the UV radiation from the central illuminating source (Öberg et al. 2008). The CH_3OH **absorption feature** is shown in Figure 17. There could be possible contribution from C_2H_5OH to the CH_3OH absorption (Boogert et al. 2008). In Figure 10 we see a narrow absorption line at 13.04 μm which we label as CH_3OCHO. The CH_3OCHO absorption is from the OCO deformation mode, which is the weakest transition of CH_3OCHO (Terwisscha van Scheltinga et al. 2021). It also is possible this narrow absorption line at 13.04 μm is an unidentified line.

YSO Y3 **also** has prominent CH_4, NH_3, CH_3OH, CH_3OCHO, and CO_2 ice absorption features. **Together with** weak PAH emission at 11.2 μm and the least number of narrow emission lines in comparison to Y1, Y2, Y4, Y6, and Y9, **this makes** Y3 the youngest protostar in this study. PAH emission as well as fine structure line emission (such as neon and sulfur which is observed in Y3) can be due to the central ionizing source or, alternatively, can also be excited due to neighboring massive stars. Y9 is slightly older than Y3 with a weak CO_2 doublet feature. YSOs Y1, Y2, and Y4 have broad silicate absorption features at 9.5 μm. It is difficult to disentangle the silicate absorption from the PAH emission at 8.5 μm and 11 μm without modeling, which will be done in a later paper. The silicate absorption along with several H_2 and fine structure line emission, but lack of any other broad ice absorption in these three YSOs suggests these are more evolved YSOs with UV radiation from the central star affecting their parental molecular gas. Y6 is the oldest YSO in this work because this source has no silicate or ice absorption features.

6. SUMMARY

We present MIRI MRS observations of 11 YSOs in the N79 region of the LMC, six of which have a full or almost-full wavelength coverage from 4.9 μm to 27.9 μm. The blended *Spitzer*-identified YSOs are resolved into multiple protostars in the MRS IFU observations in N79 East and South. The *Spitzer*-identified YSO in N79 West is a single massive source. We identify the mid-IR emission and absorption lines for the six YSOs in Tables 1 - 6 and summarize our findings:

1. **The mass inferred by fitting SED models to the *Spitzer* and *Herschel* photometry for clusters E1, S1, and S2 is 18.3 ± 2.7, 25.4 ± 3.2, and 15.7 ± 4.5 $M_\odot$. Y2 is likely the dominating source in E1, Y4 is the dominating source in S1, and Y9 is the dominating source in S2. The isolated massive protostar Y1 in W1 has a mass of 13.6 ± 1.6 $M_\odot$.**

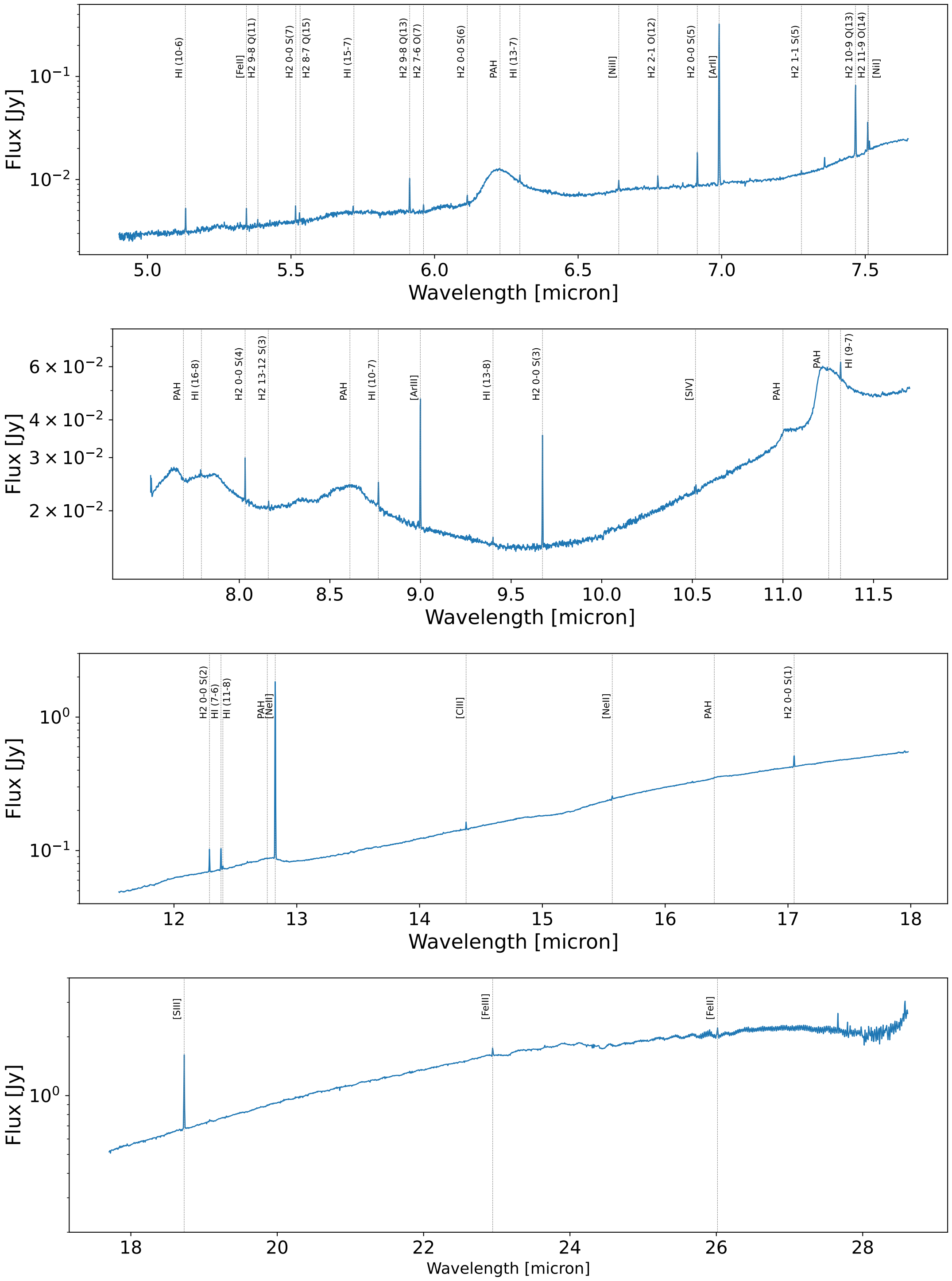

Figure 9. Spectra taken in channels 1-4 of Source Y2 in N79 East. Full line list is given in Table 2.

2. The YSOs have a variety of PAH emission lines at 6.2, 7.7, 8.6, 11.0, 11.2, 12.7, and 16.4 μm. YSOs Y1, Y2, and Y9 have all seven PAH emission features in their spectra. Y6 has the 6.2, 7.7, and 11.2 μm PAH emission feature, and Y3 only has the 11.2 μm emission. YSO Y4, the central ionizing source of SSC candidate H72.97-69.39, has no PAH features likely due to the intense radiation and strong stellar winds destroying the surrounding PAHs.

3. All six YSOs have several molecular hydrogen emission lines. Y2 located in the East GMC has 16 H_2 lines, the most number of emisison lines out of all the sources in this work. Y3, the youngest source, has five H_2 lines. The prominent absorption lines seen in the spectrum of Y3 indicate that this protostar is enshrouded by dust and the central protostar has not started ionizing the surrounding gas. The H_2 lines seen in the spectra of Y3 could be due to the dominant source, Y2, exciting the H_2.

4. [Ne II] 12.8 μm, [Ne III] 15.5 μm, [Ar II] 6.9 μm, [Ar III] 8.9 and 21.8 μm, and [Fe II] 25.9 μm emission lines indicate the presence of high-velocity shocks (>70 km s^{-1}) in Y1, Y2, Y4, Y6, and Y9. Low-velocity shocks are also present in these YSOs since we identify strong H_2 and [Cl II] emission lines. Alternatively, [Ne II] and [Ne III] emission lines can arise from nearby high-mass YSOs photo-exciting the gas with extreme UV and X-ray photons.

5. H I emission lines are often found to trace protostellar accretion and are usually abundant in H II regions. **The mass accretion rate of Y1, Y2, Y4, and Y9 range between** $3.09 \times 10^{-4} - 9.23 \times 10^{-4}$**,** $7.83 \times 10^{-4} - 1.61 \times 10^{-3}$**,** $1.01 \times 10^{-2} - 1.89 \times 10^{-2}$**,** $1.22 \times 10^{-4} - 2.69 \times 10^{-4}$ $M_\odot$ yr^{-1}**. Accretion rates as high as** 10^{-4} $M_\odot$ yr^{-1} **have been measured for low-mass stars in the Milky Way. The reason for high accretion rates inferred from H I (7-6) for YSOs in N79 could be because 1) gravitational force dominates in high-mass YSOs leading to a higher rate, and 2) shocks and winds can also contribute to the measured H I (7-6) flux leading to our calculations of the mass accretion rates to be upper-limits.**

6. ALMA observations of SO is offset by 90° from the ^{13}CO molecular gas outflows at the location of Y4. High-velocity winds > 100 km s^{-1} compressing the gas in the immediate vicinity of Y4 can explain the excess H I (7-6) and SO emission, and the low abundance of [Ne II] emission.

7. We detect solid- and gas-phase absorption features in the spectra of Y1, Y3, Y4, Y6, and Y9. YSO Y2 has no absorption features. One possible explanation for the HCN and CO_2 gas-phase absorption features in Y6 and Y9 is that high-velocity winds are heating the surrounding gas to 100 K or higher, leading to an increase in their abundances. Y3 and Y9 also have the CO_2 doublet feature, with Y3 having the most prominent absorption lines. YSO Y3 has five prominent absorption lines, likely because this source is less than 10,000 yrs old.

Table 1. Source Y1 Emission and Absorption Lines

Name	Absorption or Emission	Lab Wave [μm]	Meas Wave [μm]	Meas Wave Err [μm]	FWHM [μm]	Flux [erg s^{-1} cm^{-2}]	Flux Err [erg s^{-1} cm^{-2}]
H2 10-9 Q(2)	E	4.987	4.99115	0.00125	0.00093	8.815E-17	1.122E-16
H I (10-6)	E	5.129	5.13902	0.00138	0.00138	5.369E-17	1.070E-16
H2 5-5 S(13)	E	5.291	5.29989	0.00109	0.00129	1.005E-16	1.079E-16
[Fe II] a4F9/2-a6D9/2	E	5.340	5.34462	0.00013	0.00136	3.631E-16	1.145E-16
H2 7-6 O(6)	E	5.415	5.42082	0.00012	0.00657	3.573E-16	1.121E-16
H2 0-0 S(7)	E	5.511	5.51660	0.00100	0.00176	2.348E-16	1.030E-16
H2 9-8 Q(13)	E	5.909	5.91066	0.00174	0.00167	1.135E-16	1.231E-16
NH3	A	6.150	6.12035	0.00033	0.00437	4.060E-16	1.043E-16
PAH	E	6.200	6.22776	0.00077	0.10208	2.972E-14	7.087E-16
[Ni II] 2D3/2-2D5/2	E	6.636	6.64202	0.00122	0.00232	1.319E-16	1.029E-16
H2 0-0 S(5)	E	6.910	6.91495	0.00025	0.00208	7.061E-16	1.035E-16
[Ar II] 2P1/2-2P3/2	E	6.985	6.99076	0.00044	0.00199	3.713E-15	1.367E-16
C2H5OH	A	7.240	7.22451	0.00035	0.00661	4.094E-16	8.805E-17
H2 8-8 S(12)	E	7.323	7.33174	0.00346	0.00124	9.381E-17	9.875E-17
H2 10-9 Q(13)	E	7.452	7.46514	0.00046	0.00230	7.573E-16	1.078E-16
H2 11-9 O(14)	E	7.507	7.50931	0.00131	0.00197	1.026E-16	1.039E-16
PAH	E	7.700	7.64696	0.00649	0.12591	5.838E-14	9.781E-16
PAH	E	7.700	7.84175	0.00857	0.11913	5.252E-14	8.866E-16
H2 0-0 S(4)	E	8.025	8.03197	0.00002	0.00208	4.252E-16	2.013E-16
PAH	E	8.600	8.64508	0.00313	0.60429	1.569E-13	2.585E-15
[Ar III] 3P1-3P2	E	8.991	8.99895	0.00070	0.00294	4.512E-16	1.470E-16
H2 3-3 S(4)	E	9.431	9.43722	0.00087	0.00161	7.016E-17	1.111E-16
H2 0-0 S(3)	E	9.665	9.67298	0.00003	0.00257	9.457E-16	1.093E-16
[S IV] 2P3/2-2P1/2	E	10.511	10.51908	0.00013	0.00331	3.934E-16	1.959E-16
PAH	E	11.000	11.00937	0.01351	0.04045	2.485E-15	2.633E-15
PAH	E	11.200	11.25099	0.00086	0.12722	5.593E-14	1.194E-15
(9-7)	E	11.310	11.31906	0.00191	0.00306	3.124E-16	8.245E-17
H2 0-0 S(2)	E	12.279	12.28917	0.00042	0.00358	6.591E-16	2.709E-16
H I (7-6)	E	12.370	12.38198	0.00073	0.00458	1.289E-15	3.953E-16
PAH	E	12.700	12.759794	0.00363	0.24805	3.061E-14	1.423E-15
[Ne II] 2P1/2-2P3/2	E	12.814	12.82427	0.00052	0.00430	3.216E-14	6.875E-16
H2 5-4 O(15)	E	13.828	13.84260	0.00115	0.00306	7.150E-17	2.483E-16
[Cl II] 3P1-3P2	E	14.368	14.37880	0.00005	0.00424	3.582E-16	2.608E-16
[Ne III] 3P1-3P2	E	15.555	15.56790	0.00085	0.00640	1.750E-15	2.698E-16
PAH	E	16.400	16.43141	0.00355	0.08704	6.57E-15	8.51E-16
H2 0-0 S(1)	E	17.035	17.04974	0.00099	0.00576	2.091E-15	3.982E-16
[P III] 2P3/2-2P1/2	E	17.885	17.89816	0.00058	0.00641	3.619E-16	4.472E-16
[Fe II] a4F7/2-a4F9/2	E	17.936	17.94813	0.00201	0.00667	6.665E-16	3.848E-16
[S III] 3P2-3P1	E	18.713	18.72723	0.00178	0.00938	3.702E-14	2.742E-15
[Fe III] 5D3-5D4	E	22.925	22.94277	0.00023	0.00936	2.592E-15	2.031E-15
[Fe II] a6D7/2-a6D9/2	E	25.998	26.01579	0.00101	0.01069	8.920E-15	2.534E-15

NOTE—Column 1: Name of line. Column 2: Emission or absorption line. 'E' stands for emission and 'A' stands for absorption. Column 3: Laboratory wavelength. Column 4: Measured wavelength. Column 5: Error in measured wavelength. Column 6: FWHM of line. Column 7: Measured flux. Column 8: Error in flux.

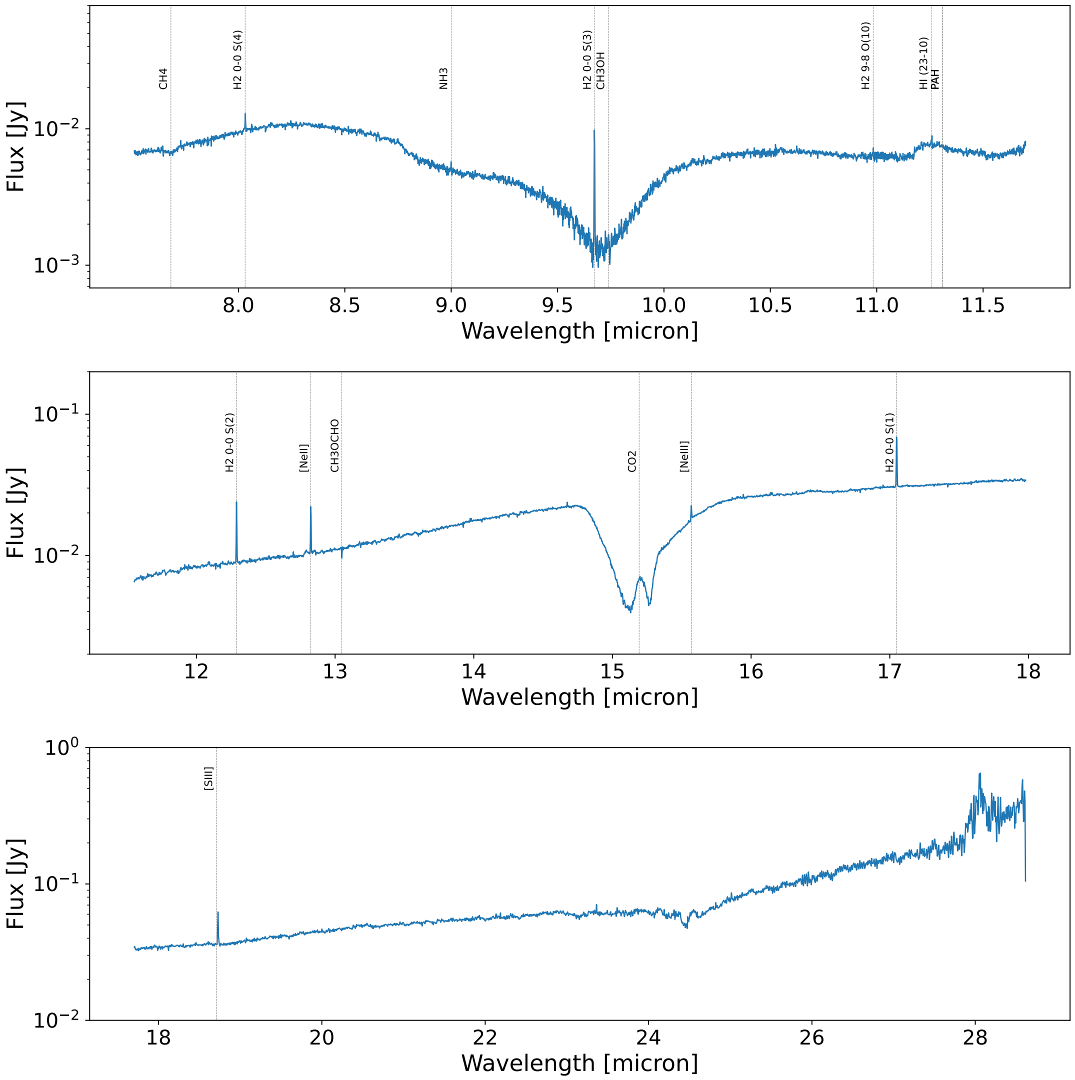

Figure 10. Spectra taken in channels 2-4 of Source Y3 in N79 East. Full line list is given in Table 3.

Table 2. Source Y2 Emission and Absorption Lines

Name	Absorption or Emission	Lab Wave [μm]	Meas Wave [μm]	Meas Wave Err [μm]	FWHM [μm]	Flux [erg s^{-1} cm^{-2}]	Flux Err [erg s^{-1} cm^{-2}]
H I (10-6)	E	5.129	5.13263	0.00057	0.00182	4.748E-16	6.219E-17
[Fe II] a4F9/2-a6D9/2	E	5.340	5.34461	0.00006	0.00137	5.551E-16	8.300E-17
H2 9-8 Q(11)	E	5.373	5.38499	0.00059	0.00167	9.680E-17	4.856E-17
H2 0-0 S(7)	E	5.511	5.51671	0.00111	0.00173	2.866E-16	4.758E-17
H2 8-7 Q(15)	E	5.540	5.53164	0.00244	0.00185	1.542E-16	4.724E-17
H I (15-7)	E	5.711	5.71989	5.71989	0.00151	1.464E-16	4.922E-17
H2 9-8 Q(13)	E	5.909	5.91320	0.00000	0.00210	8.560E-16	7.946E-17
H2 7-6 O(7)	E	5.956	5.96141	0.00021	0.00198	1.063E-16	5.994E-17
H2 0-0 S(6)	E	6.109	6.11391	0.00009	0.00205	2.376E-16	6.366E-17
PAH	E	6.200	6.22780	0.00037	0.10271	8.871E-14	9.380E-16
H I (13-7)	E	6.292	6.29757	0.00037	0.00175	2.356E-16	8.179E-17
[Ni II] 2D3/2-2D5/2	E	6.636	6.64164	0.00004	0.00214	2.863E-16	4.431E-17
H2 2-1 O(12)	E	6.776	6.77758	0.00002	0.00200	3.273E-16	4.541E-17
H2 0-0 S(5)	E	6.910	6.91527	0.00006	0.00218	1.281E-15	5.278E-17
[Ar II] 2P1/2-2P3/2	E	6.985	6.99117	0.00003	0.00200	4.019E-14	7.912E-16
H2 1-1 S(5)	E	7.280	7.27795	0.00035	0.00191	1.116E-16	4.386E-17
[Ni III] 3F4-3F34	E	7.349	7.35930	0.00089	0.00209	3.675E-16	5.095E-17
H2 10-9 Q(13)	E	7.452	7.46605	0.00035	0.00200	7.606E-15	1.727E-16
H2 11-9 O(14)	E	7.507	7.50953	0.00073	0.00207	1.951E-15	8.293E-17
[Ni I] a3F3-a3F4	E	7.507	7.51097	0.00343	0.00108	5.058E-16	6.366E-17
PAH	E	7.700	7.61215	0.01997	0.28076	3.900E-13	2.741E-15
PAH	E	7.700	7.84645	0.01984	0.21193	2.769E-13	1.968E-15
H I (16-8)	E	7.780	7.79157	0.00532	0.00269	6.172E-17	2.000E-16
H2 0-0 S(4)	E	8.025	8.03199	0.00004	0.00215	8.687E-16	1.519E-16
H2 13-12 S(3)	E	8.148	8.16010	0.00185	0.00313	1.188E-16	1.400E-16
PAH	E	8.600	8.61029	0.00532	0.23580	5.719E-14	4.092E-15
H I (10-7)	E	8.760	8.76749	0.00066	0.00326	4.637E-16	6.774E-17
[Ar III] 3P1-3P2	E	8.991	8.99889	0.00066	0.00295	3.377E-15	1.458E-16
H I (13-8)	E	9.329	9.40022	0.00027	0.00230	7.797E-17	4.239E-17
H2 0-0 S(3)	E	9.665	9.67309	0.00014	0.00239	1.748E-15	5.295E-17
[S IV] 2P3/2-2P1/2	E	10.511	10.51739	0.00286	0.00357	7.523E-17	7.825E-17
PAH	E	11.000	11.01255	0.01518	0.04319	4.270E-15	4.765E-15
PAH	E	11.200	11.25264	0.00088	0.13145	9.979E-14	2.124E-15
H I (9-7)	E	11.310	11.31796	0.00049	0.00317	1.089E-15	8.138E-17
H2 0-0 S(2)	E	12.279	12.28923	0.00048	0.00393	2.596E-15	3.061E-16
H I (7-6)	E	12.370	12.38270	0.00105	0.00545	6.634E-15	8.583E-16
H I (11-8)	E	12.387	12.39815	0.00060	0.00597	8.307E-16	2.907E-16
PAH	E	12.700	12.75113	0.00605	0.24369	5.321E-14	4.201E-15
[Ne II] 2P1/2-2P3/2	E	12.814	12.82466	0.00091	0.00493	1.617E-13	3.307E-15
[Cl II] 3P1-3P2	E	14.368	14.37897	0.00022	0.00382	8.129E-16	4.088E-16
[Ne III] 3P1-3P2	E	15.555	15.56927	0.00052	0.00569	5.001E-16	6.220E-16
PAH	E	16.400	16.44669	0.00285	0.08292	1.151E-14	1.258E-15
H2 0-0 S(1)	E	17.035	17.05001	0.00124	0.00581	4.152E-15	8.730E-16
[S III] 3P2-3P1	E	18.713	18.72859	0.00041	0.00803	7.605E-14	5.615E-15
[Fe III] 5D3-5D4	E	22.925	22.94417	0.00117	0.00992	7.756E-15	6.346E-15
[Fe II] a6D7/2-a6D9/2	E	25.998	26.01564	0.00169	0.01007	1.659E-14	8.436E-15

NOTE—Column 1: Name of line. Column 2: Emission or absorption line. 'E' stands for emission and 'A' stands for absorption. Column 3: Laboratory wavelength. Column 4: Measured wavelength. Column 5: Error in measured wavelength. Column 6: FWHM of line. Column 7: Measured flux. Column 8: Error in flux.

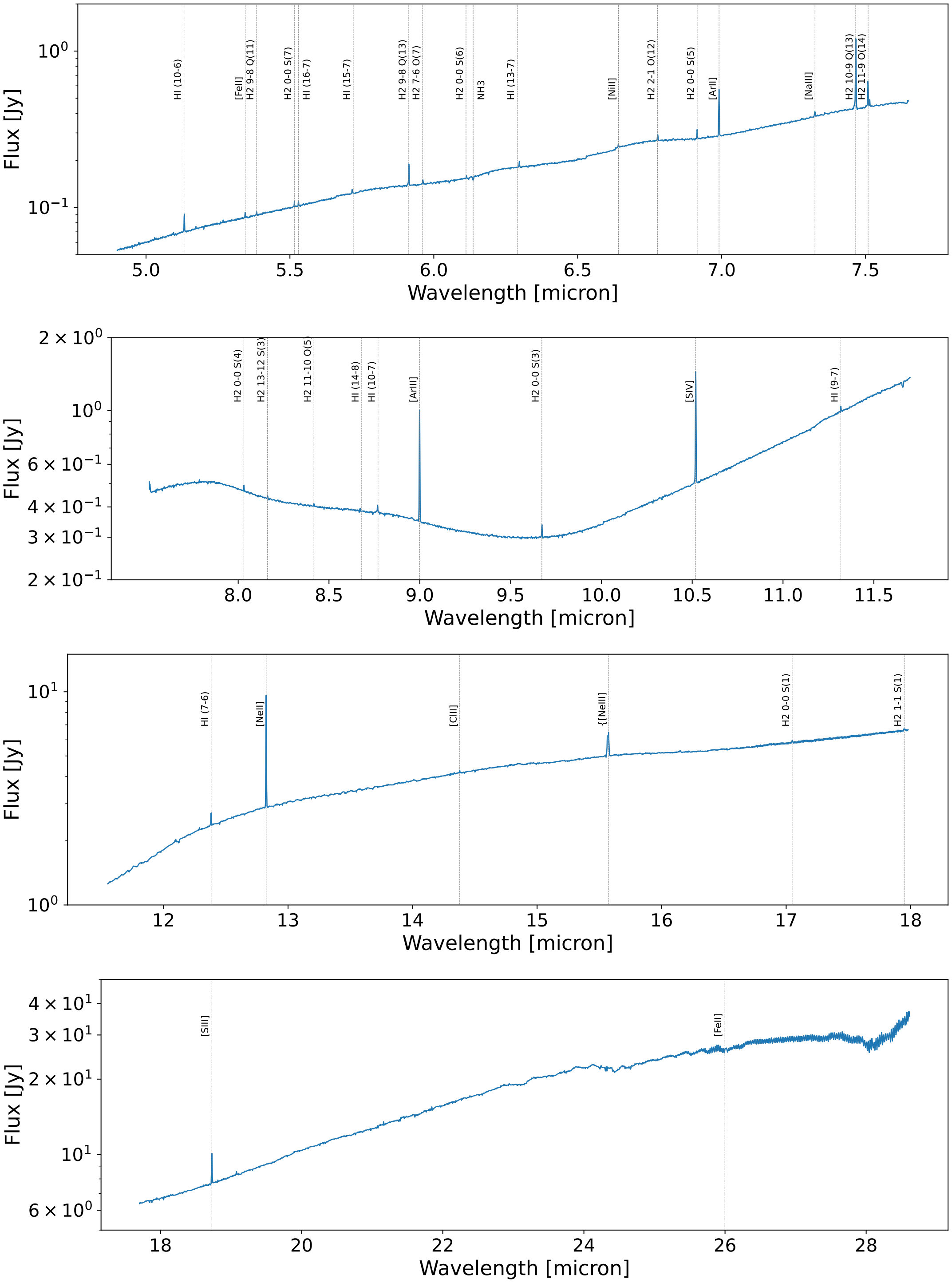

Figure 11. Spectra taken in channels 1-4 of Source Y4 in N79 South1. Full line list is given in Table 4.

Table 3. Source Y3 Emission and Absorption Lines

Name	Absorption or Emission	Lab Wave [μm]	Meas Wave [μm]	Meas Wave Err [μm]	FWHM [μm]	Flux [erg s^{-1} cm^{-2}]	Flux Err [erg s^{-1} cm^{-2}]
CH4	A	7.700	7.68265	0.00209	0.05443	3.312E-15	4.038E-16
H2 0-0 S(4)	E	8.025	8.03164	0.00031	0.00231	3.917E-16	1.183E-16
NH3	A	9.000	8.93675	0.00212	0.30607	3.524E-14	7.778E-16
H2 0-0 S(3)	E	9.665	9.67342	0.00047	0.00291	7.907E-16	2.746E-17
CH3OH	A	9.700	9.73806	0.00289	0.35165	5.140E-14	1.340E-15
H2 9-8 O(10)	E	10.974	10.97567	0.00868	0.00113	4.793E-18	4.697E-17
PAH	E	11.200	11.27072	0.00190	0.14982	1.038E-14	4.178E-16
H I (23-10)	E	11.243	11.25589	0.00405	0.00139	3.282E-17	4.861E-17
H2 0-0 S(2)	E	12.279	12.28930	0.00055	0.00425	1.393E-15	7.711E-17
[Ne II] 2P1/2-2P3/2	E	12.814	12.82459	0.00084	0.00506	1.254E-15	7.040E-17
CH3OCHO	A	13.020	13.04829	0.00046	0.00311	8.629E-17	6.287E-17
CO2	A	15.200	15.19246	0.00152	0.46127	3.636E-13	3.096E-14
[Ne III] 3P1-3P2	E	15.555	15.56852	0.00023	0.00568	2.579E-16	7.367E-17
H2 0-0 S(1)	E	17.035	17.04969	0.00094	0.00576	2.577E-15	9.930E-17
[S III] 3P2-3P1	E	18.713	18.72850	0.00056	0.00841	2.106E-15	3.365E-16

NOTE—Column 1: Name of line. Column 2: Emission or absorption line. 'E' stands for emission and 'A' stands for absorption. Column 3: Laboratory wavelength. Column 4: Measured wavelength. Column 5: Error in measured wavelength. Column 6: FWHM of line. Column 7: Measured flux. Column 8: Error in flux.

This research relied on the following resources: NASA's Astrophysics Data System and the SIMBAD and VizieR databases, operated at the Centre de Données astronomiques de Strasbourg, France. This research also made use of Astropy,[1] a community-developed core Python package for Astronomy (Astropy Collaboration et al. 2013, 2018, 2022). This work is based on observations made with the NASA/ESA/CSA James Webb Space Telescope. **The JWST data presented in this paper were obtained from the Mikulski Archive for Space Telescopes (MAST) at the Space Telescope Science Institute. The specific observations analyzed can be accessed via DOI.** These observations are associated with program #1235.

ON was supported by the Director's Discretionary Fund at the Space Telescope Science Institute and the NASA Postdoctoral Program at NASA Goddard Space Flight Center, administered by Oak Ridge Associated Universities under contract with NASA. MM and NH acknowledge that a portion of their research was carried out at the Jet Propulsion Laboratory, California Institute of Technology, under a contract with the National Aeronautics and Space Administration (80NM0018D0004). ASH is supported in part by an STScI Postdoctoral Fellowship. LL acknowledges support from the NSF through grant 2054178. OCJ acknowledges support from an STFC Webb fellowship. CN acknowledge the support of an STFC studentship. PJK acknowledges support from the Science Foundation Ireland/Irish Research Council Pathway programme under Grant Number 21/PATH-S/9360.

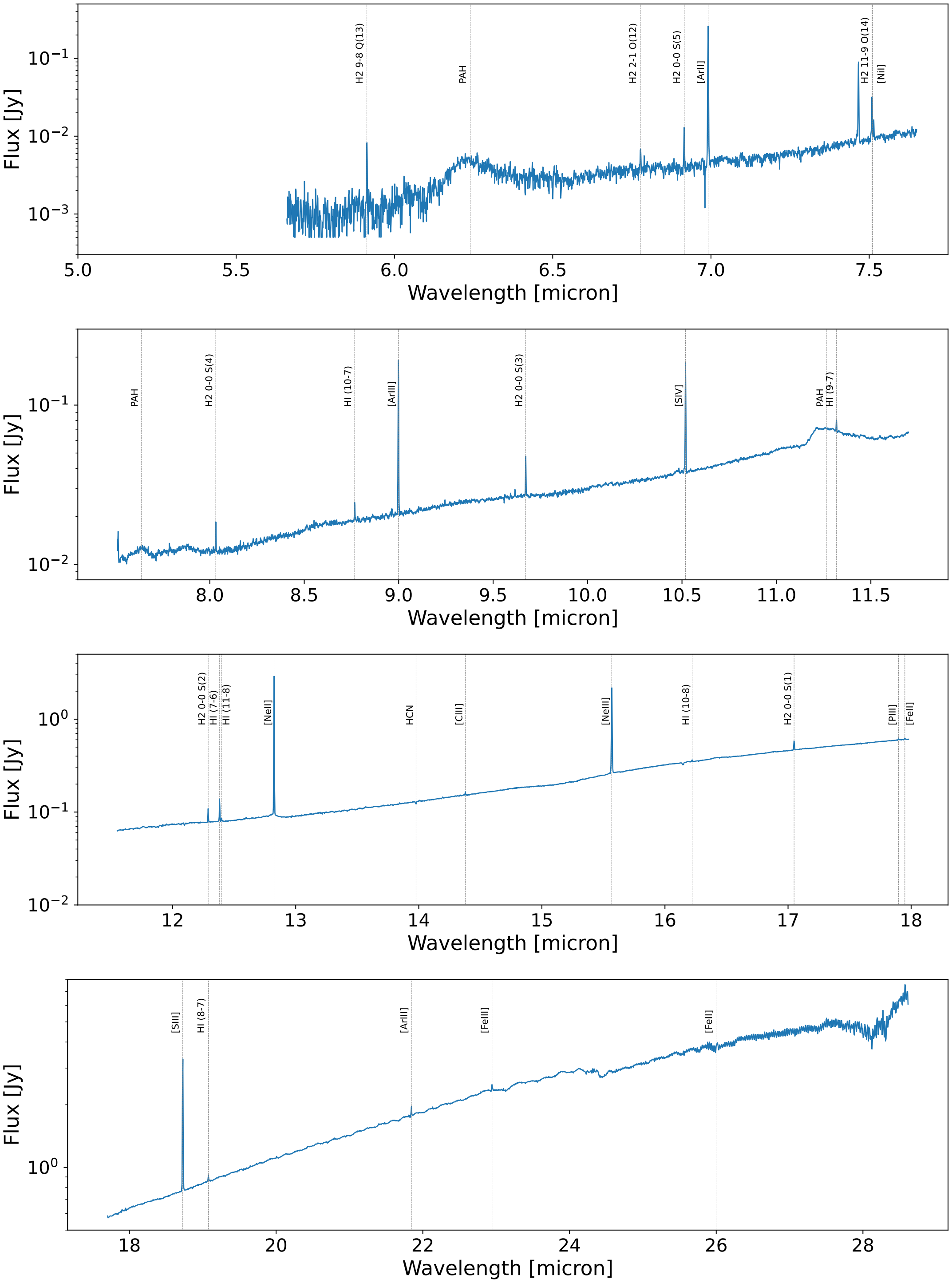

Figure 12. Spectra taken in channels 1-4 of Source Y6 in N79 South1. Full line list is given in Table 5.

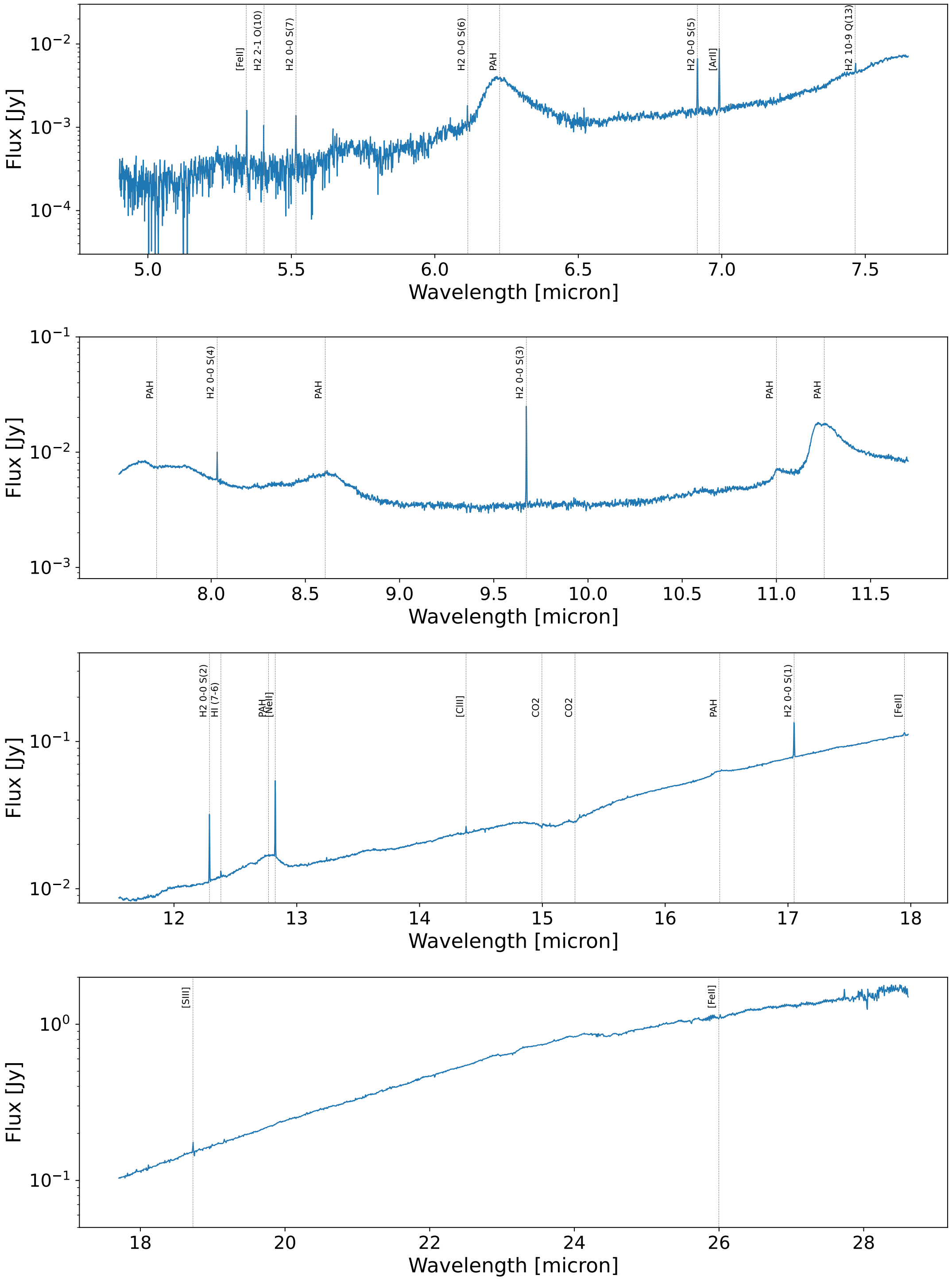

Figure 13. Spectra taken in channels 1-4 of Source Y9 in N79 South2. Full line list is given in Table 6.

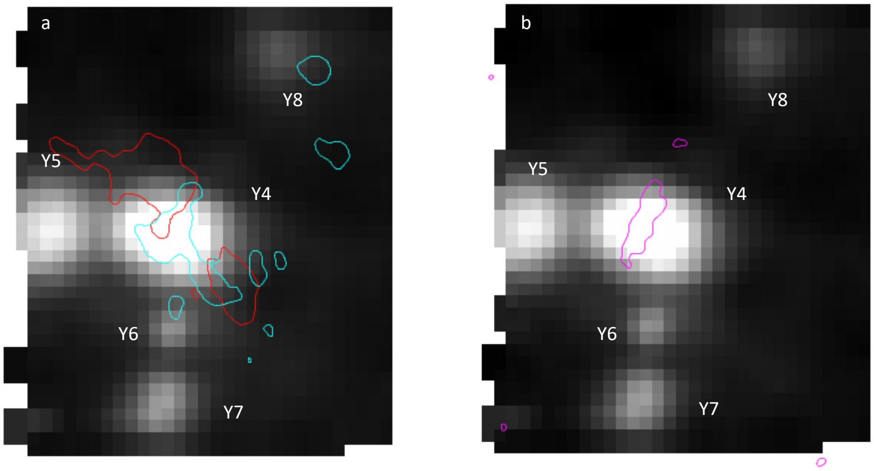

Figure 14. Left: The [Ne II] line emission slice overlaid with the ALMA ^{13}CO blue-shifted (cyan contour) and red-shifted (red contour) outflows. The outflows were determined by Nayak et al. (2019) by integrating over the line wings of the ^{13}CO spectrum. Right: The ALMA SO observations (magenta contour) shown with the MRS [Ne II] line emission slice.

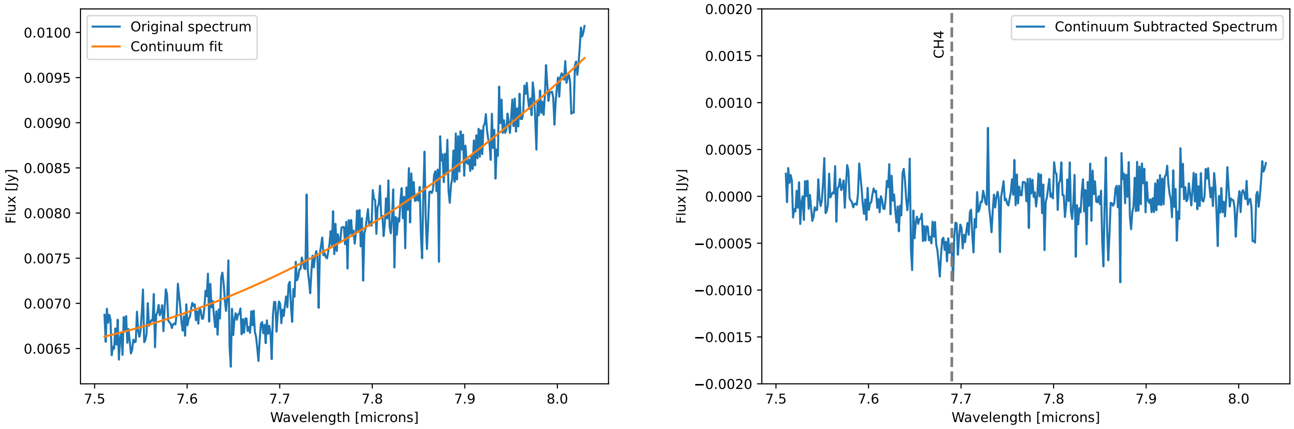

Figure 15. Left: The 7.5 − 8.6 μm MRS spectrum of Y3 and the locally fitted continuum. Right: The continuum subtracted spectrum of the CH_4 absorption feature.

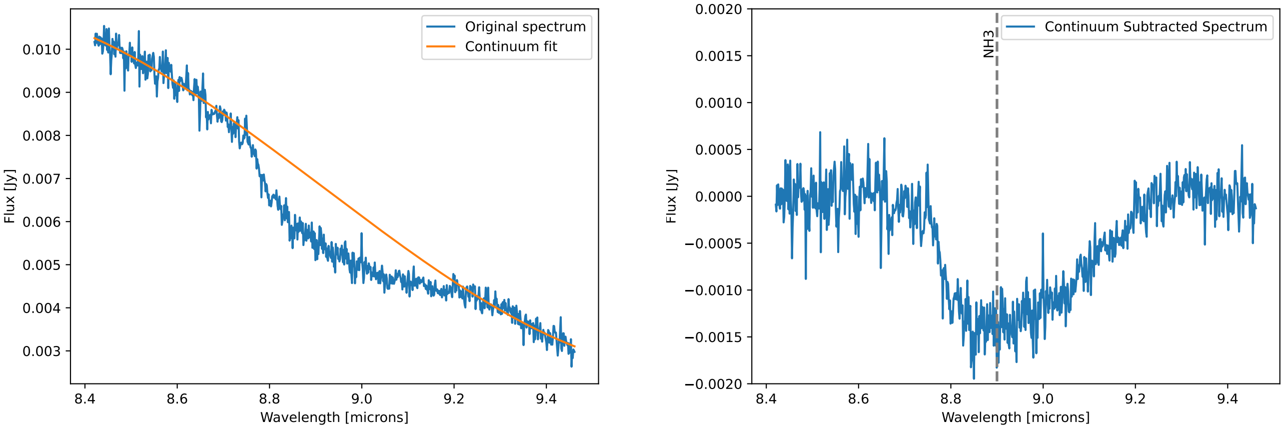

Figure 16. Left: The 8.4 − 9.4 μm MRS spectrum of Y3 and the locally fitted continuum. Right: The continuum subtracted spectrum of the NH_3 absorption feature.

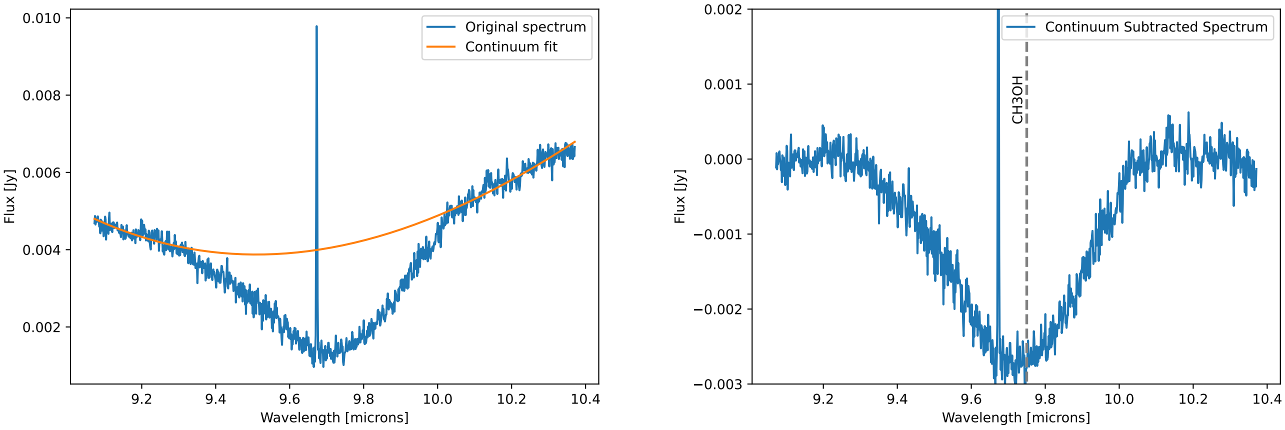

Figure 17. Left: The 9.2 − 10.4 μm MRS spectrum of Y3 and the locally fitted continuum. Right: The continuum subtracted spectrum of the CH_3OH absorption feature.

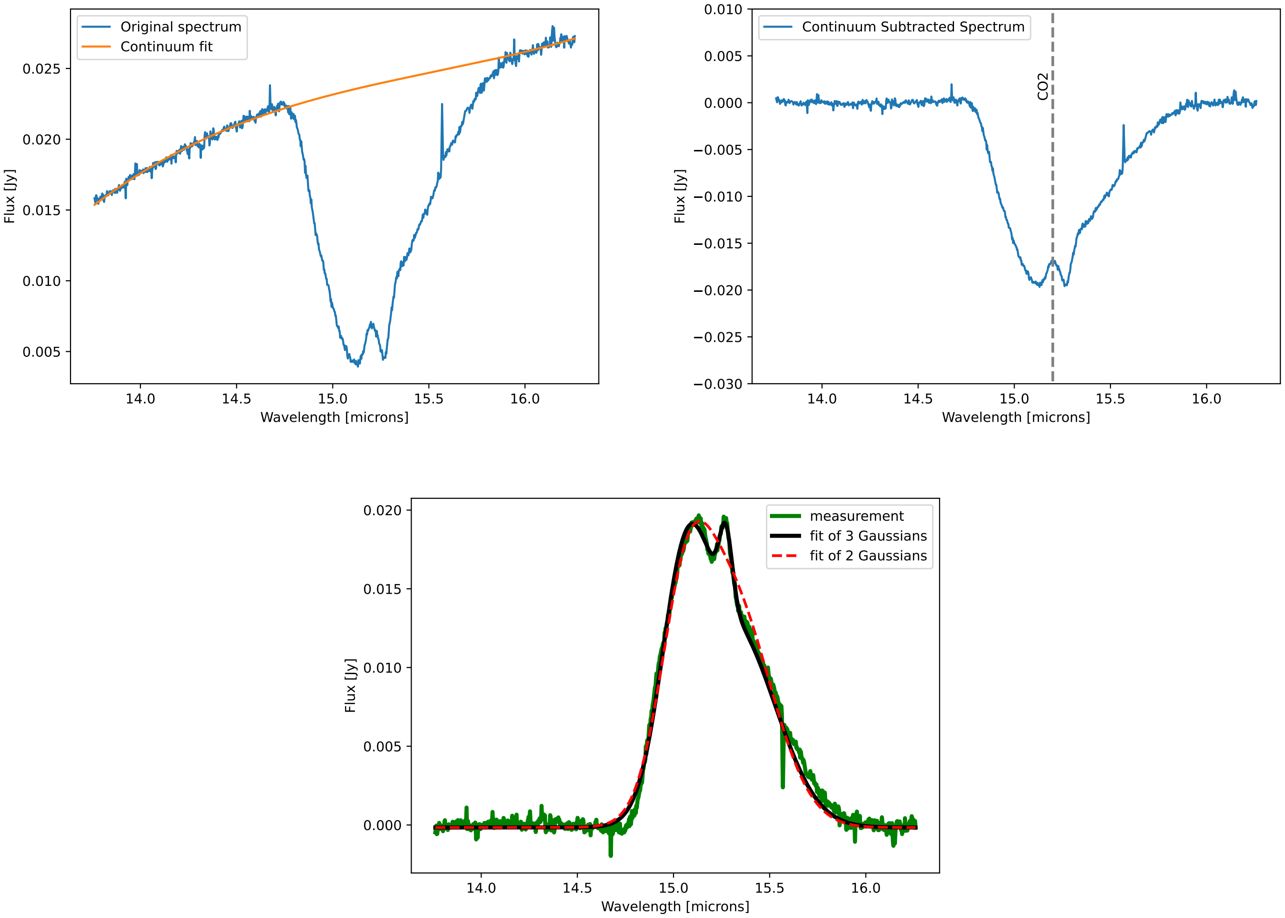

Figure 18. Top Left: The 13.8 − 16.2 μm MRS spectrum of Y3 and the locally fitted continuum. Top Right: The continuum subtracted spectrum of the CO_2 absorption feature. Bottom: We fit two and three gaussian distributions to the CO_2 mixture feature. The residual error when fitting three guassian distribution is 0.41 and the residual error when fitting two gaussian distribution is 0.53, therefore the three gaussians give a better fit to the observed absorption line. The two peaks at 15.1 μm and 15.3 μm represent a CO_2-CO and a CO_2-H_2O mixture, respectively. The broad shoulder at longer wavelengths is due to a mixture of CO_2-CH_3OH.

Table 4. Source Y4 Emission and Absorption Lines

Name	Absorption or Emission	Lab Wave [μm]	Meas Wave [μm]	Meas Wave Err [μm]	FWHM [μm]	Flux [erg s^{-1} cm^{-2}]	Flux Err [erg s^{-1} cm^{-2}]
[Fe II] a4F9/2-a6D9/2	E	5.340	5.34442	0.00010	0.00135	1.937E-15	3.752E-16
H2 9-8 Q(11)	E	5.373	5.38409	0.00031	0.00184	8.636E-16	1.003E-15
H2 0-0 S(7)	E	5.511	5.51550	0.00010	0.00118	1.086E-15	1.046E-15
H I (10-6)	E	5.129	5.13282	0.00038	0.00185	4.521E-15	1.013E-15
H I (16-7)	E	5.525	5.53040	0.00040	0.00180	1.226E-15	1.065E-15
H I (15-7)	E	5.711	5.71673	0.00034	0.00223	1.523E-15	1.406E-15
H2 9-8 Q(13)	E	5.909	5.91294	0.00026	0.00220	9.763E-15	1.486E-15
H2 7-6 O(7)	E	5.956	5.96132	0.00068	0.00212	1.346E-15	1.372E-15
H2 0-0 S(6)	E	6.109	6.11192	0.00128	0.00161	7.511E-16	1.345E-15
NH3	A	6.150	6.13673	0.00010	0.00328	2.133E-15	1.295E-15
H I (13-7)	E	6.292	6.29676	0.00044	0.00191	2.348E-15	1.498E-15
[Ni II] 2D3/2-2D5/2	E	6.636	6.64181	0.00021	0.00218	1.981E-15	1.631E-15
H2 2-1 O(12)	E	6.776	6.77762	0.00002	0.00263	4.722E-15	1.730E-15
H2 0-0 S(5)	E	6.910	6.91518	0.00002	0.00159	4.481E-15	1.668E-15
[Ar II] 2P1/2-2P3/2	E	6.985	6.99120	0.00000	0.00201	3.873E-14	2.128E-15
[Na III] 2P1/2-2P3/2	E	7.318	7.32457	0.00057	0.00363	5.462E-15	2.121E-15
H2 10-9 Q(13)	E	7.452	7.46609	0.00031	0.00216	1.026E-13	3.196E-15
H2 11-9 O(14)	E	7.507	7.50919	0.00039	0.00240	3.419E-14	2.444E-15
H2 0-0 S(4)	E	8.025	8.03148	0.00047	0.00264	2.865E-15	3.494E-15
H2 13-12 S(3)	E	8.148	8.16118	0.00077	0.00260	1.334E-15	3.333E-15
H2 11-10 O(5)	E	8.410	8.41706	0.00031	0.00282	1.340E-15	2.673E-15
H I (14-8)	E	8.665	8.68037	0.00882	0.00327	5.226E-17	2.243E-15
H I (10-7)	E	8.760	8.76765	0.00050	0.00333	4.061E-15	1.696E-15
[Ar III] 3P1-3P2	E	8.991	8.99884	0.00071	0.00335	9.191E-14	2.713E-15
H2 0-0 S(3)	E	9.665	9.67205	0.00090	0.00305	3.947E-15	9.178E-16
[S IV] 2P3/2-2P1/2	E	10.511	10.51943	0.00048	0.00355	1.068E-13	3.065E-15
H I (9-7)	E	11.310	11.31834	0.00011	0.00377	8.782E-15	2.487E-15
H I (7-6)	E	12.370	12.38235	0.00140	0.00529	7.162E-14	5.798E-15
[Ne II] 2P1/2-2P3/2	E	12.814	12.82449	0.00074	0.00490	6.398E-13	1.812E-14
[Cl II] 3P1-3P2	E	14.368	14.37854	0.00021	0.00521	1.334E-14	1.131E-14
[Ne III] 3P1-3P2	E	15.555	15.57259	0.00116	0.00815	2.250E-13	9.701E-15
H2 0-0 S(1)	E	17.035	17.04803	0.00072	0.00606	6.571E-15	8.205E-15
H2 1-1 S(1)	E	17.933	17.94781	0.00156	0.00731	7.735E-15	8.479E-15
[S III] 3P2-3P1	E	18.713	18.72804	0.00096	0.00988	2.627E-13	4.292E-14
[Fe II] a6D7/2-a6D9/2	E	25.998	26.01279	0.00467	0.01892	1.012E-13	7.918E-14

Note—Column 1: Name of line. Column 2: Emission or absorption line. 'E' stands for emission and 'A' stands for absorption. Column 3: Laboratory wavelength. Column 4: Measured wavelength. Column 5: Error in measured wavelength. Column 6: FWHM of line. Column 7: Measured flux. Column 8: Error in flux.

Table 5. Source Y6 Emission and Absorption Lines

Name	Absorption or Emission	Lab Wave [μm]	Meas Wave [μm]	Meas Wave Err [μm]	FWHM [μm]	Flux [erg s^{-1} cm^{-2}]	Flux Err [erg s^{-1} cm^{-2}]
H2 9-8 Q(13)	E	5.909	5.91289	0.00031	0.00209	1.237E-15	5.581E-17
PAH	E	6.200	6.23934	0.00168	0.12349	4.838E-14	2.093E-15
H2 2-1 O(12)	E	6.776	6.77683	0.00077	0.00248	4.536E-16	3.956E-17
H2 0-0 S(5)	E	6.910	6.91559	0.00039	0.00177	1.119E-15	4.166E-17
[Ar II] 2P1/2-2P3/2	E	6.985	6.99106	0.00014	0.00147	2.919E-14	6.152E-16
H2 11-9 O(14)	E	7.506	7.50930	0.00050	0.00233	3.471E-15	1.009E-16
[Ni I] a3F3-a3F4	E	7.507	7.51107	0.00333	0.00104	1.122E-15	6.581E-17
PAH	E	7.700	7.63727	0.03884	0.40222	1.327E-13	4.066E-14
H2 0-0 S(4)	E	8.025	8.03162	0.00033	0.00271	8.518E-16	1.387E-16
H I (10-7)	E	8.760	8.76730	0.00045	0.00278	7.269E-16	1.397E-16
[Ar III] 3P1-3P2	E	8.991	8.99845	0.00020	0.00314	2.073E-14	5.794E-16
H2 0-0 S(3)	E	9.665	9.67272	0.00023	0.00250	1.877E-15	1.568E-16
[S IV] 2P3/2-2P1/2	E	10.511	10.51874	0.00021	0.00290	1.274E-14	3.472E-16
PAH	E	11.200	11.26670	0.00103	0.16708	1.134E-13	2.218E-15
H I (9-7)	E	11.310	11.31777	0.00062	0.00322	1.940E-15	1.868E-16
H2 0-0 S(2)	E	12.279	12.28880	0.00005	0.00400	2.890E-15	4.229E-16
H I (7-6)	E	12.370	12.38179	0.00054	0.00468	1.013E-14	7.068E-16
H I (11-8)	E	12.387	12.39659	0.00034	0.00643	1.941E-15	4.093E-16
[Ne II] 2P1/2-2P3/2	E	12.814	12.82418	0.00043	0.00411	2.285E-13	4.481E-15
HCN	A	14.050	13.97779	0.00044	0.00806	1.757E-15	3.056E-16
[Cl II] 3P1-3P2	E	14.368	14.37792	0.00083	0.00459	1.223E-15	4.779E-16
[Ne III] 3P1-3P2	E	15.555	15.56774	0.00101	0.00652	1.422E-13	1.609E-15
H I (10-8)	E	16.209	16.22067	0.00058	0.00703	1.552E-15	6.704E-16
H2 0-0 S(1)	E	17.035	17.04911	0.00036	0.00524	5.884E-15	7.255E-16
[P III] 2P3/2-2P1/2,	E	17.885	17.89809	0.00066	0.00781	1.078E-15	7.461E-16
[Fe II] a4F7/2-a4F9/2	E	17.936	17.94888	0.00125	0.00725	2.028E-15	1.110E-15
[S III] 3P2-3P1	E	18.713	18.72739	0.00161	0.00939	2.311E-13	8.686E-15
H I (8-7)	E	19.062	19.07710	0.00010	0.00786	3.549E-15	5.163E-15
[Ar III] 3P0-3P1	E	21.830	21.84428	0.00072	0.00761	7.731E-15	5.142E-15
[Fe III] 5D3-5D4	E	22.925	22.94357	0.00056	0.00943	5.923E-15	5.517E-15
[Fe II] a6D7/2-a6D9/2	E	25.998	26.01276	0.05576	0.02060	5.419E-14	4.615E-13

Note—Column 1: Name of line. Column 2: Emission or absorption line. 'E' stands for emission and 'A' stands for absorption. Column 3: Laboratory wavelength. Column 4: Measured wavelength. Column 5: Error in measured wavelength. Column 6: FWHM of line. Column 7: Measured flux. Column 8: Error in flux.

Table 6. Source Y9 Emission and Absorption Lines

Name	Absorption or Emission	Lab Wave [μm]	Meas Wave [μm]	Meas Wave Err [μm]	FWHM [μm]	Flux [erg s^{-1} cm^{-2}]	Flux Err [erg s^{-1} cm^{-2}]
[Fe II] a4F9/2-a6D9/2	E	5.340	5.34445	0.00007	0.00163	4.549E-16	6.039E-17
H2 2-1 O(10)	E	5.409	5.40474	0.00114	0.00094	8.026E-17	6.885E-18
H2 0-0 S(7)	E	5.511	5.51611	0.00168	0.12349	4.838E-14	2.093E-15
H2 0-0 S(6)	E	6.109	6.11485	0.00077	0.00248	4.536E-16	3.956E-17
PAH	E	6.200	6.22564	0.00046	0.10209	3.688E-14	5.239E-16
H2 0-0 S(5)	E	6.910	6.91506	0.00039	0.00177	1.119E-15	4.166E-17
[Ar II] 2P1/2-2P3/2	E	6.985	6.99097	0.00014	0.00147	2.919E-14	6.152E-16
H2 10-9 Q(13)	E	7.452	7.46467	0.00173	0.00206	1.097E-16	2.175E-17
PAH	E	7.700	7.71042	0.00167	0.42496	1.743E-13	2.186E-15
H2 0-0 S(4)	E	8.025	8.03178	0.00050	0.00233	3.471E-15	1.009E-16
PAH	E	8.600	8.60527	0.00469	0.25788	4.374E-14	2.523E-15
H2 0-0 S(3)	E	9.665	9.67303	0.00333	0.00104	1.122E-15	6.581E-17
PAH	E	11.000	11.01046	0.01876	0.05358	3.006E-15	3.343E-15
PAH	E	11.200	11.25369	0.00079	0.13108	5.634E-14	1.079E-15
H2 0-0 S(2)	E	12.279	12.28889	0.03883	0.40231	1.327E-13	4.065E-14
H I (7-6)	E	12.370	12.38211	0.00033	0.00271	8.518E-16	1.387E-16
PAH	E	12.700	12.76987	0.00636	0.22928	3.827E-14	3.371E-15
[Ne II] 2P1/2-2P3/2	E	12.814	12.82475	0.00020	0.00314	2.073E-14	5.794E-16
[Cl II] 3P1-3P2	E	14.368	14.37866	0.00023	0.00250	1.877E-15	1.568E-16
CO2	A	14.970	14.99625	0.00070	0.00829	2.811E-16	7.555E-17
CO2	A	15.200	15.26561	0.00195	0.03826	1.150E-15	1.866E-16
PAH	E	16.400	16.44424	0.00113	0.14098	1.159E-14	2.950E-16
H2 0-0 S(1)	E	17.035	17.04970	0.00095	0.00603	4.074E-15	1.134E-16
[Fe II] a4F7/2-a4F9/2	E	17.936	17.94714	0.00110	0.00915	6.789E-16	2.811E-16
[S III] 3P2-3P1	E	18.713	18.72798	0.00021	0.00290	1.274E-14	3.472E-16
[Fe II] a6D7/2-a6D9/2	E	25.998	26.01709	0.04723	0.00944	4.592E-15	5.425E-14

NOTE—Column 1: Name of line. Column 2: Emission or absorption line. 'E' stands for emission and 'A' stands for absorption. Column 3: Laboratory wavelength. Column 4: Measured wavelength. Column 5: Error in measured wavelength. Column 6: FWHM of line. Column 7: Measured flux. Column 8: Error in flux.

Table 7. Summary of Emission and Absorption Lines Observed in YSOs

Name	6.2 μm PAH	7.7 μm PAH	8.6 μm PAH	11.0 μm PAH	11.2 μm PAH	12.7 μm PAH	16.4 μm PAH	CO$_2$ Absorp Line	No. of Other Absorp. Lines	No. of H I Lines	No. of Fine Sturcture Lines	No. of H$_2$ Lines
Y1	✓	✓	✓	✓	✓	✓	✓		2	2	13	15
Y2	✓	✓	✓	✓	✓	✓	✓		0	9	13	16
Y3					✓			✓	4	1	3	5
Y4									1	8	11	15
Y6	✓	✓			✓				1	6	13	8
Y9	✓	✓	✓	✓	✓	✓	✓	✓	1	1	7	9

APPENDIX

We describe the emission and absorption lines that we could not identify in more detail in Table A1.

REFERENCES

Alcalá, J. M., Natta, A., Manara, C. F., et al. 2014, A&A, 561, A2

Astropy Collaboration, Robitaille, T. P., Tollerud, E. J., et al. 2013, A&A, 558, A33

Astropy Collaboration, Price-Whelan, A. M., Sipőcz, B. M., et al. 2018, AJ, 156, 123

Astropy Collaboration, Price-Whelan, A. M., Lim, P. L., et al. 2022, ApJ, 935, 167

Bally, J. 2016, ARA&A, 54, 491

Barnes, A. T., Longmore, S. N., Dale, J. E., et al. 2020, MNRAS, 498, 4906

Bauschlicher, Charles W., J., Peeters, E., & Allamandola, L. J. 2008, ApJ, 678, 316

Beltrán, M. T., Cesaroni, R., Neri, R., & Codella, C. 2011, A&A, 525, A151

Beuther, H., Churchwell, E. B., McKee, C. F., & Tan, J. C. 2007, in Protostars and Planets V, ed. B. Reipurth, D. Jewitt, & K. Keil, 165

Boogert, A. C. A., Pontoppidan, K. M., Knez, C., et al. 2008, ApJ, 678, 985

Boonman, A. M. S., van Dishoeck, E. F., Lahuis, F., & Doty, S. D. 2003a, A&A, 399, 1063

Boonman, A. M. S., van Dishoeck, E. F., Lahuis, F., et al. 2003b, A&A, 399, 1047

Bushouse, H., Eisenhamer, J., Dencheva, N., et al. 2023, JWST Calibration Pipeline

Calvet, N., Muzerolle, J., Briceño, C., et al. 2004, AJ, 128, 1294

Chen, C. H. R., Chu, Y.-H., Gruendl, R. A., Gordon, K. D., & Heitsch, F. 2009, ApJ, 695, 511

Churchwell, E. 2002, in Astronomical Society of the Pacific Conference Series, Vol. 267, Hot Star Workshop III: The Earliest Phases of Massive Star Birth, ed. P. Crowther, 3

Codella, C., Cabrit, S., Gueth, F., et al. 2014, A&A, 568, L5

De Marchi, G., Paresce, F., Panagia, N., et al. 2011, ApJ, 739, 27

Draine, B. T., & Li, A. 2001, ApJ, 551, 807

Draine, B. T., & McKee, C. F. 1993, ARA&A, 31, 373

Draine, B. T., Dale, D. A., Bendo, G., et al. 2007, ApJ, 663, 866

Drew, J. E., Bunn, J. C., & Hoare, M. G. 1993, MNRAS, 265, 12

Esplugues, G. B., Tercero, B., Cernicharo, J., et al. 2013, A&A, 556, A143

Feast, M. 1999, in New Views of the Magellanic Clouds, ed. Y. H. Chu, N. Suntzeff, J. Hesser, & D. Bohlender, Vol. 190, 542

Gardner, J. P., Mather, J. C., Abbott, R., et al. 2023, PASP, 135, 068001

Gerakines, P. A., Whittet, D. C. B., Ehrenfreund, P., et al. 1999, ApJ, 522, 357

Grebel, E. K., & Chu, Y.-H. 2000, AJ, 119, 787

Gruendl, R. A., & Chu, Y.-H. 2009, ApJS, 184, 172

Gullbring, E., Hartmann, L., Briceño, C., & Calvet, N. 1998, ApJ, 492, 323

Herczeg, G. J., & Hillenbrand, L. A. 2008, ApJ, 681, 594

Higdon, S. J. U., Armus, L., Higdon, J. L., Soifer, B. T., & Spoon, H. W. W. 2006, ApJ, 648, 323

Hollenbach, D. 1997, in Herbig-Haro Flows and the Birth of Stars, ed. B. Reipurth & C. Bertout, Vol. 182, 181–198

Hollenbach, D., & Gorti, U. 2009, ApJ, 703, 1203

Hollenbach, D. J., Chernoff, D. F., & McKee, C. F. 1989, in Infrared Spectroscopy in Astronomy, ed. E. Böhm-Vitense, 245

Hony, S., Van Kerckhoven, C., Peeters, E., et al. 2001, A&A, 370, 1030

Hudgins, D. M., Bauschlicher, C. W., J., & Sandford, S. A. 2004, ApJ, 614, 770

Hunter, D. A., Shaya, E. J., Scowen, P., et al. 1995, ApJ, 444, 758

Joblin, C., Tielens, A. G. G. M., Allamandola, L. J., & Geballe, T. R. 1996, ApJ, 458, 610

Kaufman, M. J., & Neufeld, D. A. 1996, ApJ, 456, 611

Knight, C., Peeters, E., Stock, D. J., Vacca, W. D., & Tielens, A. G. G. M. 2021, ApJ, 918, 8

Kwan, J., & Fischer, W. 2011, MNRAS, 411, 2383

Labiano, A., Azzollini, R., Bailey, J., et al. 2016, in Society of Photo-Optical Instrumentation Engineers (SPIE) Conference Series, Vol. 9910, Observatory Operations: Strategies, Processes, and Systems VI, ed. A. B. Peck, R. L. Seaman, & C. R. Benn, 99102W

Lacy, J. H., Jaffe, D. T., Zhu, Q., et al. 2007, ApJL, 658, L45

Lahuis, F., van Dishoeck, E. F., Boogert, A. C. A., et al. 2006, ApJL, 636, L145

Table A1. Unknown Emission and Absorption Lines

Source	E or A	Meas Wave	Line Origin
Y1	E	6.25882	combination of residual fringing, noise, and residual dark
Y1	E	6.25921	combination of residual fringing, noise, and residual dark
Y1	E	6.32363	does not look Nyquist sampled so likely due to a bad or warm pixel missed by outlier detection
Y1	A	16.18125	due to ‘gaps’ during the cube building process
Y2	E	23.65548	does not look Nyquist sampled so likely due to a bad or warm pixel missed by outlier detection
Y3	E	14.67484	does not look Nyquist sampled so likely due to a bad or warm pixel missed by outlier detection
Y3	E	23.36319	does not look Nyquist sampled so likely due to a bad or warm pixel missed by outlier detection
Y3	A	24.45185	residual fringe feature in overlapping region 4B/4C where the fringe flat is not great
Y4	A	11.65905	detector effect where this absorption is seen in channel 2C but not channel 3A
Y6	A	16.15000	similar to effect seen in Y1 where it is due to ‘gaps’ during the cube building process
Y9	A	14.53375	does not look Nyquist sampled so likely due to a bad or warm pixel missed by outlier detection

NOTE—Column 1: Name of YSO. Column 2: Emission or absorption line. ‘E’ stands for emission and ‘A’ stands for absorption. Column 3: Measured Wavelength. Column 4: Origin of the line.

Lambert-Huyghe, A., Madden, S. C., Lebouteiller, V., et al. 2022, A&A, 666, A112

Looney, L. W., Tobin, J. J., & Fields, B. D. 2006, ApJ, 652, 1755

Lopez, L. A., Krumholz, M. R., Bolatto, A. D., et al. 2014, ApJ, 795, 121

McKee, C. F., & Ostriker, E. C. 2007, ARA&A, 45, 565

Meixner, M., Gordon, K. D., Indebetouw, R., et al. 2006, AJ, 132, 2268

Meixner, M., Panuzzo, P., Roman-Duval, J., et al. 2013, AJ, 146, 62

Méndez-Delgado, J. E., Esteban, C., García-Rojas, J., et al. 2021a, MNRAS, 502, 1703

Méndez-Delgado, J. E., Henney, W. J., Esteban, C., et al. 2021b, ApJ, 918, 27

Morisset, C., Schaerer, D., Bouret, J. C., & Martins, F. 2004, A&A, 415, 577

Morisset, C., Schaerer, D., Martín-Hernández, N. L., et al. 2002, A&A, 386, 558

Mouri, H., Kawara, K., & Taniguchi, Y. 2000, ApJ, 528, 186

Nayak, O., Meixner, M., Sewiło, M., et al. 2019, ApJ, 877, 135

Nayak, O., Meixner, M., Okada, Y., et al. 2021, ApJ, 907, 106

Öberg, K. I., Boogert, A. C. A., Pontoppidan, K. M., et al. 2008, in Organic Matter in Space, ed. S. Kwok & S. Sanford, Vol. 251, 127–128

Öberg, K. I., Fraser, H. J., Boogert, A. C. A., et al. 2007, A&A, 462, 1187

Ochsendorf, B. B., Zinnecker, H., Nayak, O., et al. 2017, Nature Astronomy, 1, 784

Ogle, P., Boulanger, F., Guillard, P., et al. 2010, ApJ, 724, 1193

O’Halloran, B., Satyapal, S., & Dudik, R. P. 2006, ApJ, 641, 795

Oliveira, J. M., van Loon, J. T., Chen, C. H. R., et al. 2009, ApJ, 707, 1269

Oliveira, J. M., van Loon, J. T., Sloan, G. C., et al. 2013, MNRAS, 428, 3001

Pabst, C., Higgins, R., Goicoechea, J. R., et al. 2019, Nature, 565, 618

Pabst, C. H. M., Goicoechea, J. R., Teyssier, D., et al. 2020, A&A, 639, A2

Peeters, E., Bauschlicher, Charles W., J., Allamandola, L. J., et al. 2017, ApJ, 836, 198

Peeters, E., Hony, S., Van Kerckhoven, C., et al. 2002, A&A, 390, 1089

Pontoppidan, K. M., Boogert, A. C. A., Fraser, H. J., et al. 2008, ApJ, 678, 1005

Reiter, M., Nayak, O., Meixner, M., & Jones, O. 2019, MNRAS, 483, 5211

Rieke, G. H., Ressler, M. E., Morrison, J. E., et al. 2015, PASP, 127, 665

Rigliaco, E., Pascucci, I., Duchene, G., et al. 2015, ApJ, 801, 31

Robitaille, T. P. 2017, A&A, 600, A11

Rodgers, S. D., & Charnley, S. B. 2003, ApJ, 585, 355

Sabbi, E., Anderson, J., Lennon, D. J., et al. 2013, AJ, 146, 53

Schutte, W. A., Boogert, A. C. A., Tielens, A. G. G. M., et al. 1999, A&A, 343, 966

Seale, J. P., Looney, L. W., Chu, Y.-H., et al. 2009, ApJ, 699, 150

Seale, J. P., Meixner, M., Sewiło, M., et al. 2014, AJ, 148, 124

Shannon, M. J., Stock, D. J., & Peeters, E. 2016, ApJ, 824, 111

Simcoe, R. A., Burgasser, A. J., Schechter, P. L., et al. 2013, PASP, 125, 270

Simpson, J. P., Cotera, A. S., Burton, M. G., et al. 2012, MNRAS, 419, 211

Smith, J. D. T., Draine, B. T., Dale, D. A., et al. 2007, ApJ, 656, 770

Stock, D. J., Peeters, E., Tielens, A. G. G. M., Otaguro, J. N., & Bik, A. 2013, ApJ, 771, 72

Terwisscha van Scheltinga, J., Marcandalli, G., McClure, M. K., Hogerheijde, M. R., & Linnartz, H. 2021, A&A, 651, A95

Tielens, A. G. G. M. 2008, ARA&A, 46, 289

Tielens, A. G. G. M., & Hagen, W. 1982, A&A, 114, 245

Tielens, A. G. G. M., Meixner, M. M., van der Werf, P. P., et al. 1993, Science, 262, 86

van Dishoeck, E. F., & Blake, G. A. 1998, ARA&A, 36, 317

Walch, S., Whitworth, A. P., Bisbas, T. G., Wünsch, R., & Hubber, D. A. 2013, MNRAS, 435, 917

Whitney, B. A., Sewilo, M., Indebetouw, R., et al. 2008, AJ, 136, 18

Wright, G. S., Rieke, G. H., Glasse, A., et al. 2023, PASP, 135, 048003

Yang, Y.-L., Green, J. D., Pontoppidan, K. M., et al. 2022, ApJL, 941, L13

Zapata, L. A., Ho, P. T. P., Schilke, P., et al. 2009, ApJ, 698, 1422